## ARTICLE

# Radial contractility of actomyosin rings facilitates axonal trafficking and structural stability

Tong Wang[1,2,3], Wei Li[1,3], Sally Martin[1,3], Andreas Papadopulos[1], Merja Joensuu[1], Chunxia Liu[2], Anmin Jiang[1], Golnoosh Shamsollahi[1], Rumelo Amor[1], Vanessa Lanoue[1], Pranesh Padmanabhan[1], and Frédéric A. Meunier[1]

**Most mammalian neurons have a narrow axon, which constrains the passage of large cargoes such as autophagosomes that can be larger than the axon diameter. Radial axonal expansion must therefore occur to ensure efficient axonal trafficking. In this study, we reveal that the speed of various large cargoes undergoing axonal transport is significantly slower than that of small ones and that the transit of diverse-sized cargoes causes an acute, albeit transient, axonal radial expansion, which is immediately restored by constitutive axonal contractility. Using live super-resolution microscopy, we demonstrate that actomyosin-II controls axonal radial contractility and local expansion, and that NM-II filaments associate with periodic F-actin rings via their head domains. Pharmacological inhibition of NM-II activity significantly increases axon diameter by detaching the NM-II from F-actin and impacts the trafficking speed, directionality, and overall efficiency of long-range retrograde trafficking. Consequently, prolonged NM-II inactivation leads to disruption of periodic actin rings and formation of focal axonal swellings, a hallmark of axonal degeneration.**

## Introduction

Neurons are polarized cells that contain many nerve terminal boutons separated from the cell body by a long and thin axon. Tightly regulated axonal cargo transport is pivotal for neuronal development, communication, and survival (Barford et al., 2017; Tojima and Kamiguchi, 2015). Despite the heavy trafficking, quantitative EM studies have found that thin axons (inner diameter <1 µm) are the most abundant type in the mammalian central nervous system (CNS; Liewald et al., 2014; Perge et al., 2012). For instance, the long-range connective axons found in the human corpus callosum have an average diameter that ranges from 0.64 µm to 0.74 µm (Liewald et al., 2014). In contrast, the size of axonal cargoes is highly variable, encompassing autophagosomes (0.5–1.5 µm; Mizushima et al., 2002), mitochondria (0.75–3 µm; McBride et al., 2006), and endosomes (50 nm–1 µm; Altick et al., 2009). Thus, the range of cargo sizes is comparable to, or surprisingly even larger than, some of the CNS axons themselves. This advocates for the existence of radial contractility in the axons, which would allow the transient expansion of axon caliber and facilitate the passage of large cargoes. Indeed, the expansion of axonal diameter surrounding large cargoes, i.e., autophagosomes (Wang et al., 2015) or

mitochondria (Yin et al., 2016), has been observed by super-resolution microscopy and 3D EM in both normal and degenerating axons (Giacci et al., 2018; Maia et al., 2015). Considering the spatial constriction exerted by the rigid and stable circumventing axonal membrane (Abouelezz et al., 2019a; Qu et al., 2017; Zhang et al., 2017; Zhong et al., 2014), the trafficking of large cargoes is likely to be affected. In fact, a simulation study predicted that cargo trafficking was impeded by the friction from the axonal walls in small-caliber axons (Wortman et al., 2014), and correlations between axon diameter and axon trafficking have been recently reported in *Drosophila melanogaster* (Fan et al., 2017; Narayanareddy et al., 2014) and rodent neurons (Leite et al., 2016; Pesaresi et al., 2015). However, direct evidence showing whether and how axonal radial contractility affects cargo trafficking is still lacking.

We hypothesized that the underlying structural basis for axonal radial contractility is the subcortical actomyosin network, which is organized into specialized structures called membrane-associated periodic cytoskeletal structures (MPSs), as revealed with super-resolution microscopy along the shafts of mature axons (Xu et al., 2013). F-actin, together with adducin

[1]Clem Jones Centre for Ageing Dementia Research, Queensland Brain Institute, The University of Queensland, Brisbane, Australia;   [2]School of Life Science and Technology, ShanghaiTech University, Shanghai, China;   [3]The Australian Institute for Bioengineering and Nanotechnology, The University of Queensland, Brisbane, Australia.

Correspondence to Frédéric A. Meunier: f.meunier@uq.edu.au;   Tong Wang: wangtong@shanghaitech.edu.cn

and spectrin, forms a subcortical lattice with an ~190-nm periodic interval covering the majority of the axon length (Han et al., 2017; Xu et al., 2013). Disrupting axonal F-actin or spectrin leads to disassembly of MPSs (He et al., 2016; Huang et al., 2017; Zhong et al., 2014), which initiates axonal degeneration (Unsain et al., 2018; Wang et al., 2019). In addition, the depletion of adducin causes progressive dilation of the axon diameter and axon loss, accompanied by slightly impaired axonal trafficking (Leite et al., 2016). The fact that adducin knockout axons are still capable of decreasing the diameter of actin rings over time suggests the existence of additional actin regulatory machineries that maintain this constriction. Indeed, the dynamic contractility of the subcortical actomyosin network depends on nonmuscle myosin II (NM-II; Even-Ram et al., 2007; Papadopulos et al., 2015; Salbreux et al., 2012). In neurons, the activated regulatory light chain of NM-II (p-MRLC; Berger et al., 2018; Evans et al., 2017), as well as Tropomyosin isoform Tpm 3.1 (Abouelezz et al., 2019b *Preprint*), which activates and recruits NM-II to actin fibers (Bryce et al., 2003; Gateva et al., 2017), has recently been shown to coexist in periodic patterns with the actin MPS to maintain the function and structure of the axon initial segment (AIS; Berger et al., 2018). Understanding how the dynamic cytoskeletal architecture coordinates the radial axonal contractility and cargo trafficking is therefore warranted.

In this study, we combined live-imaging confocal microscopy and microfluidic techniques to examine the correlation between the speed of axonal cargoes undergoing long-range transport and their size. We found that the speed inversely correlates with the cargo size. Next, using time-lapse super-resolution structured illumination microscopy (SR-SIM), we found that both the axonal plasma membrane and the underlying actin rings undergo dynamic local deformation during the passage of large cargoes, which promotes a transient expansion immediately followed by constriction. We further demonstrated that this transient change in axon diameter is controlled by NM-II activity and that NM-II filaments closely associate with periodic actin rings via their heavy-chain head domain. Our results suggest that CNS axons are under constitutive radial constriction, which limits their diameter. Accordingly, short-term inhibition of NM-II activity with either blebbistatin (Kovács et al., 2004) or ML-7 (Saitoh et al., 1987) does not affect the periodicity of actin rings but effectively decreases their contractility and tilting angle, thereby expanding the axonal diameter. As a result of augmented axon diameter, blebbistatin increases both the speed of directed large cargoes and the back-and-forth movements of undirected ones. This leads to a transient increase in cargo mobility at the expense of overall trafficking efficacy. Prolonged NM-II inactivation by either NM-II siRNA or transfection of an MRLC loss-of-function mutant disrupts the MPS structure and leads to the formation of focal axon swelling (FAS), a hallmark of axonal degeneration.
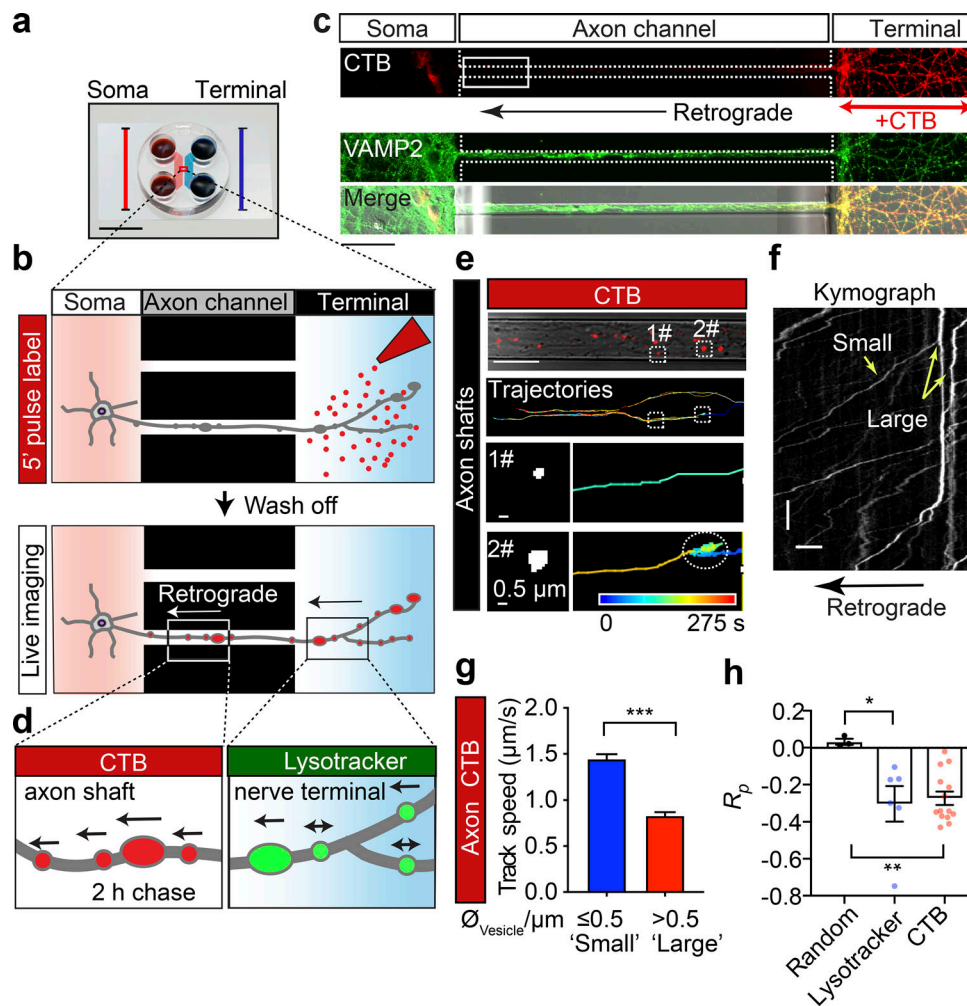
## Results

### The speed of retrograde axonal cargoes is inversely correlated with their size.

Large axonal cargoes such as endosomes, lysosomes, autophagosomes, and mitochondria tend to accumulate in FAS under

pathological conditions (Tammineni et al., 2017), suggesting that the size of cargoes might alter the axonal trafficking efficacy. To determine the relationship between the size of cargoes and their transport speed, we analyzed the speeds of various-sized retrograde lysosomal and endosomal vesicles. These cargoes were generated and fluorescently labeled with the lysosomal marker Lysotracker or the endosomal marker cholera toxin subunit B (CTB) at the nerve terminals and underwent retrograde trafficking along the axon bundles of live hippocampal neurons cultured in microfluidic devices (Fig. 1, a and b). Hydrostatic pressure was used to restrict the labeling reagents to the terminal chamber during the 5-min pulse labeling (Fig. 1 c). This was followed by a thorough wash in culture medium to remove the excess fluorescent probe and confocal time-lapse imaging and automatic tracing of the fluorescently tagged cargoes as previously described (Joensuu et al., 2017; Wang et al., 2015, 2016). To investigate different stages of axonal trafficking, live imaging was performed in two distinct axonal regions: (1) the axon shafts adjacent to the soma chamber (Fig. 1 d, left) and (2) within the terminal chamber (Fig. 1 d, right). Lysotracker-labeled vesicles detected in the nerve terminal chamber exhibited very confined movements (Fig. S1 a and Video 1). We further quantified the average speed of these tracks, which were sorted into two different groups according to their diameter (Fig. S1 a, bottom panels). We observed that vesicles with a large diameter ("large," diameter >0.5 µm) moved significantly slower (0.115 ± 0.039 µm/s) than those with a smaller diameter ("small," diameter ≤0.5 µm; 0.159 ± 0.006 µm/s), as shown in Fig. S1 b. This suggests that transport of large axonal cargoes in axons surrounding nerve terminals could be impeded during their transit. To specifically investigate the correlation between the size of axonal cargoes and their active transport speed, we further examined the trafficking speed of long-range CTB-positive retrograde carriers in the soma-proximal axon channels (Fig. 1, e–g). Consistent with our previous study (Joensuu et al., 2016), these long-range carriers exhibited a much greater trafficking speed (0.974–1.659 µm/s) than the carriers at nerve terminals (0.115–0.159 µm; see Fig. 1 g and Fig. S1, b–d). Similar to the lysosomes in the nerve terminals, the trafficking speed of these CTB-positive carriers also inversely correlated with their diameter, with small-diameter cargoes moving faster (1.44 ± 0.05 µm/s) than large-diameter ones (0.83 ± 0.04 µm/s; Fig. 1 g and Video 2; see also Fig. S1, c and d). We then examined the correlation between cargo size and speed by plotting the apparent diameter of either lysosomal carriers or CTB-positive carriers against their speed. This revealed a negative correlation, with a Pearson's coefficient of −0.303 ± 0.095 and −0.273 ± 0.036 between cargo diameter and trafficking speed in the terminal (Fig. 1 h, Lysotracker) and proximal (Fig. 1 h, CTB) axons, respectively, indicating that the speed of the trafficked cargoes declines as the cargo size increases.

### Transit of large cargoes causes a significant transient radial expansion of the axonal plasma membrane and the underneath periodic actin rings

Each organelle undergoing retrograde axonal transport is driven by multiple dyneins, which are stochastically activated and

Wang et al.
NM-II facilitates axonal trafficking and stability

Journal of Cell Biology 2 of 19
https://doi.org/10.1083/jcb.201902001

Figure 1. **The speed of retrograde axonal transport cargoes is inversely correlated with their size. (a)** Microfluidic chambers isolate unidirectional axon bundles (scale bar = 1 cm; adapted from Xonamicrofluidics.com). **(b)** Schematic diagram of the pulse-chase labeling process. Cultured hippocampal neurons were grown in a microfluidic device for DIV14. The nerve terminal chamber was incubated with fluorescently tagged CTB (50 ng/ml) for 5 min or Lysotracker (50 nM) for 30 min (pulse) after thorough washes and a 2-h chase. **(c)** Representative images of cultured neurons, showing the restriction of retrograde CTB surface labeling to nerve terminals and the position of the observation window (white box). Scale bar = 50 µm. **(d)** The axonal retrograde transport of CTB or Lysotracker was monitored at the level of the proximal axon shafts or in the nerve terminal chamber, respectively. **(e)** Time-lapse images of CTB carriers. Top: CTB labeling and tracing trajectories within the axon channels. Trajectories of small (1#, diameter ≤0.5 µm) and large (2#, diameter >0.5 µm) carriers are magnified in the bottom panels, respectively. **(f)** Representative kymographs of CTB-positive cargoes along a single axon, depicting track displacements of small and large carriers. x bar = 10 µm; y bar = 10 s. **(g)** Grouped analysis of the average speeds of CTB cargoes with small (≤ 0.5 µm) and large (>0.5 µm) diameters. Data represent mean ± SEM (small, $n$ = 248, large $n$ = 287 tracks from three independent preparations; ***, $P < 0.001$, two-tailed unpaired $t$ test). **(h)** Pearson's coefficient of the speed and diameter of retrograde Lysotracker-positive and CTB-positive cargoes. Data represent mean ± SEM from three independent preparations (random, $n$ = 3 simulated datasets; Lysotracker, $n$ = 6; CTB, $n$ = 14; $n$ represents the number of axon channels analyzed; the single value of the average correlation coefficient between the size and speed of all trajectories in each axon channel was calculated and used for the plot). Three independent groups of Gaussian-distributed random numbers were generated using the normrnd function of MATLAB. *, $P < 0.05$; **, $P < 0.01$, two-tailed unpaired $t$ test.

collectively drive cargo transport through the axonal cytosol (Chowdary et al., 2015; Mallik et al., 2005; Rai et al., 2013). Given the low viscosity of axonal cytosol, the force generated by co-operative dyneins is sufficient to ensure their retrograde trafficking through the axon (Chowdary et al., 2015). Thus, the reduced speed of the larger cargoes we observed is unlikely due to insufficient driving force or a higher viscous load due to their larger size. Considering the recent evidence suggesting the role of axon diameter in axon cargo trafficking (Fan et al., 2017; Leite et al., 2016; Narayanareddy et al., 2014), we hypothesized that

size-dependent friction on the axonal cargoes comes from the constrictive force exerted by the axonal plasma membrane, which is more likely to impede the transport of larger retrograde cargoes.

To test this hypothesis, we examined the diameter of axons in the presence or absence of cargoes at the ultrastructural level. To eliminate confounding factors related to the analysis of dendrites, experiments were only performed on axonal bundles formed within the channels of microfluidic devices (Joensuu et al., 2017; Wang et al., 2015, 2016), as shown in Fig. 2 a. We
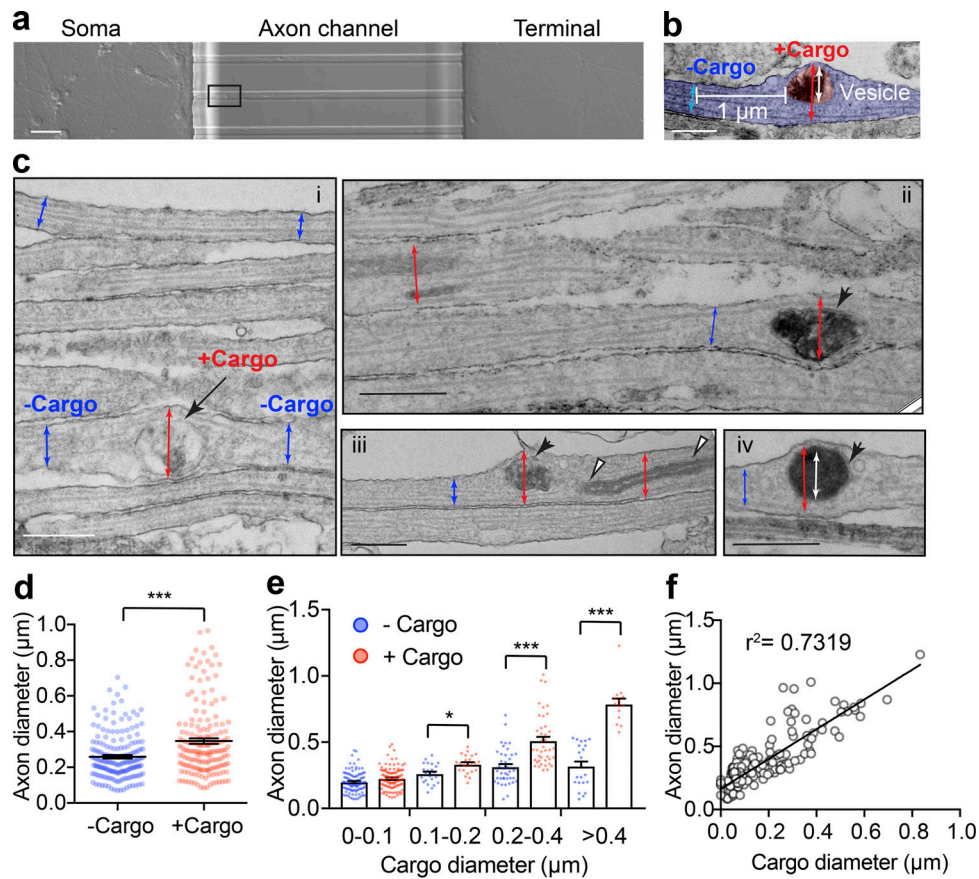
Figure 2. **The size of axonal cargoes correlates with the diameter of the axon. (a)** Bright-field image of DIV14 rat hippocampal neurons cultured in a microfluidic device with the region selected for EM outlined. Scale bar = 250 µm. **(b)** Representative electron micrographs showing the axonal diameter measurements with cargo (red) or without cargo (blue) and the associated cargo size (white). Scale bar = 0.5 µm. **(c)** Electron micrographs of axon bundles from hippocampal neurons cultured in microfluidic devices. i–iv: Axon diameters with and without cargo are marked with red and blue arrows, respectively. i: Endosome (black arrow). i–iii: Mitochondria (white arrowheads) and autophagosome (black arrowheads). Iv: Inner diameters of cargoes are marked with white arrows. Scale bars = 500 nm. **(d)** Quantification of axon diameters with cargo and without cargo. Data represent mean ± SEM, n = 182 (+ Cargo) and 182 (− Cargo) measurements from two independent preparations (***, P < 0.001, two-tailed paired $t$ test). **(e)** Grouped quantification of axonal diameter as a function of binned vesicle size. Data represent mean ± SEM; for the + Cargo group from left to right: n = 104, 23, 41, and 14 measurements; for the − Cargo group from left to right: n = 104, 23, 41, and 22 measurements. Data are from two independent preparations (*, P < 0.05; ***, P < 0.001, two-tailed unpaired $t$ test). **(f)** Cross-correlation analysis of cargo size and axonal diameter. Linear regressions were performed with the 182 paired measurements of axonal and cargo diameters of the + Cargo group. Data are from two independent preparations.

first used EM to visualize the morphology of both axon shafts and their internal cargoes. As demonstrated in Fig. 2, b and c, on the parallel axonal bundles, the diameters of axons were indeed significantly increased around large cargoes, such as large endosomes (Fig. 2 c i, arrow), mitochondria (Fig. 2 c iii, white arrowheads) and autophagosomes (Fig. 2 c, iii and iv, black arrowheads). When we measured the diameter of the axonal segment with (red) and without cargo (blue) in the same axon, we found that those with cargoes had a significantly larger diameter (347 ± 15.6 nm) than those without cargoes (259 ± 9.4 nm; Fig. 2 d) with paired comparison. We also observed that as the size of the cargoes increased, the extent of axon expansion also increased proportionally (Fig. 2, e and f), suggesting that the stretch of the axon membrane is indeed caused by the transiting cargo.

We next investigated the effect of transiting cargoes on the diameter of axons in live hippocampal neurons. To effectively label the subcortical actomyosin network in axons, we used Lifeact-GFP, a peptide that binds to both actin filaments (F-actin) and cytosolic actin monomers (Riedl et al., 2008). Similar to a previous study (Ganguly et al., 2015), with the resolution of SIM, we detected Lifeact-GFP distribution in both the filamentous and cytosolic fractions in axons of live hippocampal neurons; we also observed various-sized intraaxonal "fluorescence voids" that likely represent axoplasmic organelles (Fig. 3 a), which are known to exclude actin from their lumens (Gormal et al., 2015). Similar to cargo-induced axon dilation observed with EM, the axon diameter was also significantly expanded in axon segments containing these unlabeled organelles (Fig. 3 b). We then characterized the nature of these organelles by comparing their localization with that of various organelle markers resolved by 3D SIM and found substantial overlap with autophagosomes (Fig. S2 a, LC3-mRFP) late endosomes (Fig. S2 b, Rab7-mRFP), and mitochondria (Fig. S2 c, Mito-TagRFP). This suggests that these
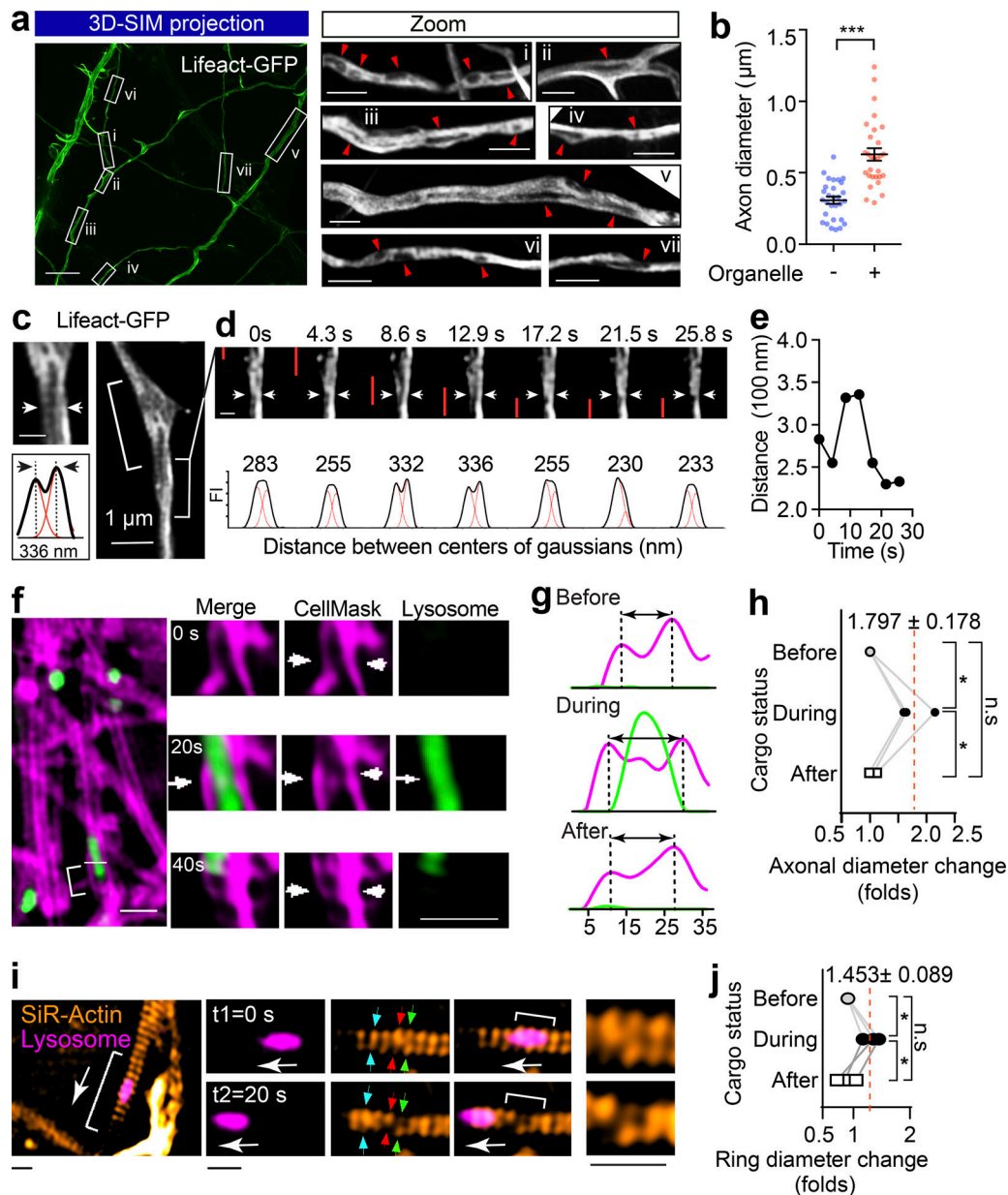
**Figure 3. The passage of large axonal cargoes causes a transient radial expansion of the axon. (a)** Rat hippocampal neurons were transfected with Lifeact-GFP and imaged with 3D SIM. Left: Representative maximum projection of 3D SIM of Lifeact-GFP expressing axons are shown. Scale bar = 5 µm. Right: Magnified ROIs in left panel. Arrowheads indicate fluorescence voids with low Lifeact-GFP signals within the axon. Scale bar = 1 µm. **(b)** Quantification of axon diameters with (+) and without (−) unlabeled organelles. Data represent mean ± SEM from three independent preparations (+ black hole, $n$ = 29, − black hole, $n$ = 29 axons; ***, P < 0.001, two-tailed unpaired $t$ test). **(c)** Rat hippocampal neurons cultured in a glass-bottom dish were transfected with Lifeact-GFP (DIV12) and imaged by time-lapse SIM (DIV14). Representative live axons with unlabeled cargoes passing through are shown, with inset demonstrating the Gaussian fittings of the annotated line transection of axon. Scale bar = 0.5 µm (inset). **(d)** Time-lapse images of bracketed region in c, showing the axonal diameter fluctuation as the cargo (indicated with red bar) transits. **(e)** Plot of the distance between axon membranes against time. **(f)** Representative time-lapse dual-color SIM of live axons with plasma membrane labeled with CellMask and Lysosome with Lysotracker red. The deformations of plasma membrane trigged by the passage of lysosome (arrows) are indicated with arrowheads. Scale bar = 2 µm. **(g)** Line transection of axon plasma membrane annotated with blue arrows. **(h)** Quantification of axonal diameter changes as cargoes pass through. Data represent mean ± SEM from three axons (*, P < 0.05, two-tailed paired $t$ test). **(i)** Representative time-lapse dual-color SIM of live axons with periodic actin rings labeled with SiR-actin and Lysosome with Lysotracker red. The deformations of actin rings trigged by the passage of lysosome are indicated with arrows and zoomed in the inlets. Scale bars = 0.5 µm. **(j)** Quantification of actin ring diameter changes as cargoes pass through. Data represent mean ± SEM from three axons (*, P < 0.05, two-tailed paired $t$ test). n.s., not significant.

organelles caused significant local dilation of the axon (Fig. S2 d). To further investigate whether these organelles were cargoes that associate with the retrograde transport machinery, we determined their colocalization with markers of retrograde

carriers, such as terminal-derived CTB (Wang et al., 2016) and the neuron-specific dynein intermediate chain 1B (DIC[1B]; Ha et al., 2008). These organelles partially overlapped with CTB- and DIC[1B]-positive axonal structures (Fig. S2, e and f), indicating

that a substantial portion of them were indeed caused by retrograde trafficking organelles in live axons.

Next, we investigated whether the transit of cargoes correlated with the local axon dilation in live neurons using time-lapse SIM. In Lifeact-GFP–expressing axons, using unbiased Gaussian fitting (Fig. 3 c), we assessed the fluctuations in axon diameter and clearly detected radial diameter expansion through the transient separation of the two lateral axonal membranes, which caused an increase in the distance between the center of the Gaussians (Fig. 3 d and Video 3). This effect was transient, and the initial diameter was restored after the passage of the unlabeled organelles, as shown in Fig. 3 e. Similarly, we used CellMask to label the axonal plasma membrane and found that an axonal diameter expansion occurred concomitantly with the passage of Lysotracker-positive cargoes (Fig. 3, f–h; and Videos 4 and 5). Interestingly, this cargo-induced radial expansion was also observed in the SiR-actin–labeled periodic actin rings (Fig. 3, i and j; and Videos 6 and 7). Taken together, our results demonstrate that passage of axonal cargoes could cause transient radial expansion of the axonal diameter, including both plasma membrane and underlying periodic actin rings in live neurons.

## NM-II controls the radial contractility of the periodic actin rings along the axon

The contractility and plasma membrane tension are controlled by the actomyosin-II network, which is composed of NM-II filaments sliding upon F-actin; Arnold and Gallo, 2014; Berger et al., 2018; Evans et al., 2017). This interaction can be disrupted by blebbistatin, a specific membrane-permeable inhibitor that blocks the ATPase activity of the myosin heavy chain (MHC) and detaches NM-II from F-actin (Kovács et al., 2004), as shown in Fig. 4 a. To explore the molecular basis of the axonal radial contractility, we first sought to resolve the actomyosin structures along the axon shafts. To specifically label actin MPS in live neurons, we employed SiR-actin, a far-red fluorescent probe that has high brightness and low cytotoxicity (Lukinavičius et al., 2013, 2014) to label the F-actin along the axon. We used time-lapse SIM, which had previously been used to accurately visualize axon MPS in live neurons (Qu et al., 2017), to visualize the periodic axon actin rings along live axons (Fig. 4 b and Video 8). We found MPS formed along the axon shaft has a conserved longitudinal spacing of ~190 nm (193.2 ± 0.15 nm; Fig. 4 c), which is similar to the spacing distance observed in fixed and Phalloidin-647–labeled axons (191.8 ± 2.3 nm; Fig. S3, a–d). These values were similar to those previously reported in rat hippocampal axons (He et al., 2016; Xu et al., 2013). As NM-II is involved in the regulation of axonal diameter (Fan et al., 2017) and associated with the MPS in axons (Berger et al., 2018), we also examined whether blocking NM-II activity using blebbistatin would affect the spacing of actin MPS. We found that 60 min of blebbistatin treatment (10 µM) had no effect on the spacing (Fig. 4 c and Fig. S3, a–e). However, this short-term NM-II inactivation significantly increased the radial diameters of actin rings in treated axons (Fig. 4 d and Fig. S3 f) and also decreased the contractility of actin MPS, as reflected in decreased ring diameter fluctuations over 20 s in live axons (Fig. 4 e).

Similar effects on axonal diameter expansion were also observed in fixed axons labeled using Phalloidin-647 (Fig. S4, a and b). Moreover, the effect of blebbistatin was reversible, as reflected by the partially recovered diameter of periodic actin rings following blebbistatin washout in SiR-actin–labeled live axons (Fig. S4, c and d). In addition, viability of treated neurons was unaffected by blebbistatin treatment (Fig. S4, e and f). The significant dilation of periodic actin rings caused by detaching NM-II suggests that the interaction between NM-II and periodic actin rings controls the radial contractility of axons. Interestingly, we found that blebbistatin treatment also affected the orientation of actin rings by decreasing their tilting angles with the axonal axis (Fig. 4 f). This suggests NM-II is likely to exert tension between adjacent actin rings.

As shown in Fig. 5 a, the local contractile activity of NM-II was also controlled by the MRLC, which is phosphorylated on conserved sites and is critical for the formation of periodic actin rings in the AIS (Berger et al., 2018). To further explore the activity of NM-II on axon radial contractility, we used ML-7 and Calyculin A, which inhibit and activate the NM-II, respectively, by controlling MRLC phosphorylation levels (Kato et al., 1988; Saitoh et al., 1987). Efficacy of ML-7 and Calyculin A treatment was confirmed by Western blotting using a specific MRLC diphosphorylation antibody (p-MRLC). Blebbistatin, the MHC ATPase inhibitor (Kovács et al., 2004), has no effect on p-MRLC levels (Fig. 5 b). Along the axons of SiR-actin–labeled live neurons, we found that ML-7 treatment (10 µM, 30 min), which inhibits NM-II activity, significantly expanded the diameter of periodic actin rings (Fig. 5, c and d), an effect similar to that of blebbistatin. To our surprise, Calyculin A treatment (50 nM, 30 min), which activates NM-II, had no significant effect on the diameter of periodic actin rings (Fig. 5 d). Both ML-7 and Calyculin A affected the actin ring tilting angle (Fig. 5 e), but not their spacing (Fig. 5 f). To further investigate the correlation between p-MRLC and axonal diameter, we also examined the correlation between endogenous p-MRLC levels and axon diameter (Fig. S5 a). We found no significant correlation (Fig. S5 b). These data show that raising NM-II activity by targeting MRLC does not change the diameter of actin rings, whereas inhibiting NM-II activity significantly increases their diameter, indicating that axonal NM-II is highly activated, which is likely to exert a constant tension on the abutting axon plasma membrane.

## NM-II closely associates with periodic actin rings along the axon

To assess the relationship between NM-II and periodic actin rings along the axon shaft, we used dual-color 3D SIM to investigate the distribution of endogenous NM-II and actin rings. We colabeled the axons of 14 d in vitro (DIV14) to DIV28 rat hippocampal neurons using SiR-actin or Phalloidin and an antibody that recognizes either the N-terminus head domain (αNM-II(nt)) or the C-terminus rod domain of NM-IIB (αNM-II(ct)), which is the dominant form of NM-II in mature axons (Berger et al., 2018; Fig. 6 a). Following fixation and permeabilization, the number of axonal segments displaying periodic actin rings was reduced (Fig. 6, b and c). We therefore
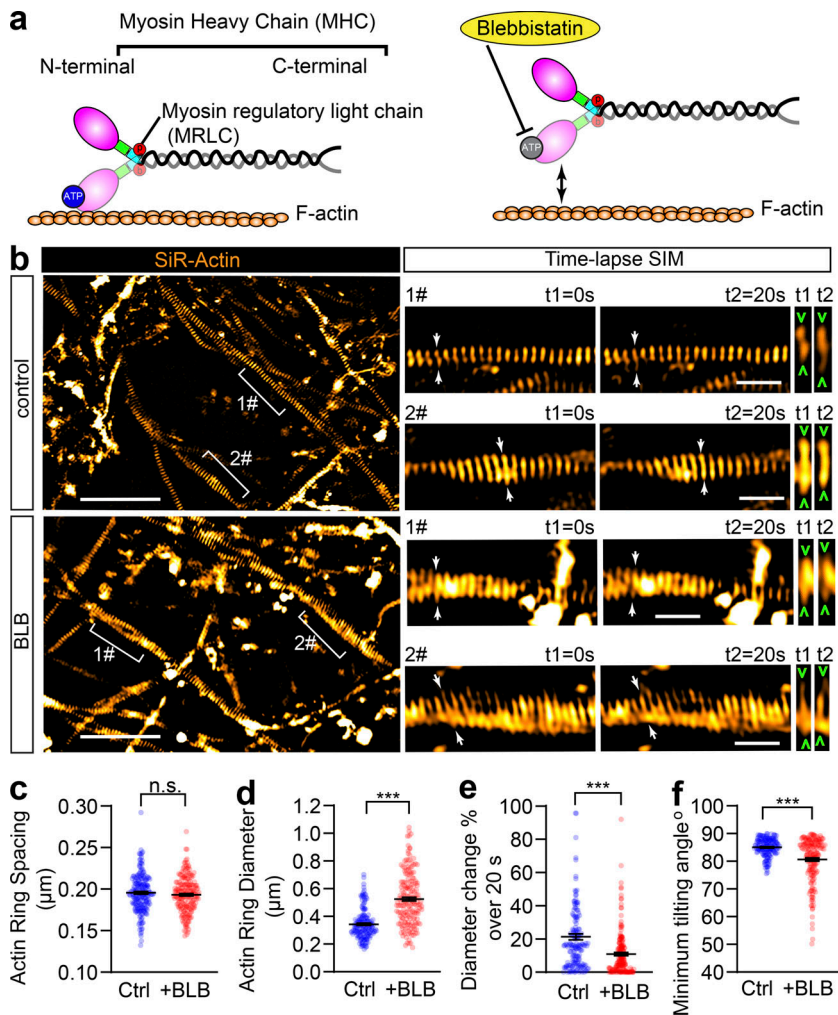
Figure 4. **Short-term inactivation of NM-II affects the diameter and angle of axonal actin rings, but not their periodic spacing. (a)** Cartoon showing the organization of actomyosin structure in nonmuscle cells, with the ATP-binding site in the head domain of MHC annotated. Blebbistatin blocks NM-II ATPase activity leading to its detachment from F-actin. **(b)** In cultured hippocampal neurons, endogenous periodic axonal actin rings were labeled using SiR-actin and live imaged using 2D SIM. Representative time-lapse SIM images of axonal actin rings are shown before (control) and after short-term blebbistatin treatment (10 µM, 30–60 min). Bracketed regions are magnified in right panels. Dynamic diameter changes of actin rings are annotated with arrowheads. Scale bars = 5 µm (left) and 1 µm (right). **(c–f)** Quantification of the spacing (c), diameter (d), fluctuation of actin ring diameter (e), and minimum tilting angles (f) of the periodic actin rings along the axon. Data represent mean ± SEM, n = 167 (control) and 186 (blebbistatin [+BLB]), representing numbers of axonal actin rings analyzed. Values were measured from three independent cultures (***, P < 0.001, two-tailed unpaired t test). n.s., not significant.

restricted our analysis of NM-II and actin dual labeling to the axonal segments with preserved periodic actin rings.

Using the αNM-II(nt), which detects the head domains of NM-II filaments (Fig. 6 a), we observed an extensive colocalization between the αNM-II(nt) puncta and periodic actin rings labeled with SiR-actin (Fig. 6 d). In contrast, αNM-II(ct) (rod domain of NM-II filaments) immunostaining (Fig. 6 a) displayed less overlap with periodic actin rings (Fig. 6 d), as compared with αNM-II(nt) (Fig. 6 e). We also quantified the spacing between adjacent NM-II puncta along the longitudinal axis of the axon, and found that both αNM-II(ct)– and αNM-II(nt)–stained puncta exhibited a periodic distribution (Fig. 6 d, arrowheads) with an average spacing of ~200 nm (212.9 ± 5.27 nm, αNM-II(nt); 218.3 ± 4.13 nm, αNM-II(nt); in Fig. 6 f). These values are similar to the periodicity of the actin rings (Xu et al., 2013) and also consistent with that of phosphorylated-MRLC periodicity, as reported recently (Berger et al., 2018).

We next investigated whether the distribution pattern of NM-II was affected by the inhibition of its activity and found that short-term blebbistatin treatment did not significantly alter the NM-II periodicity (Fig. 6, g and h) but significantly decreased the degree of colocalization between NM-II and actin MPS (Fig. 6 i). This was most apparent with the reduced colocalization between NM-II and actin voxels, as rendered by Imaris surface

function of 3D SIM images following blebbistatin treatment (Fig S6, a and b). Indeed, NM-II and actin rings distributed more discretely from each other in blebbistatin-treated axons (Fig. 6 g, left panels), as expected due to NM-II detachment from actin rings following blebbistatin inhibition.

To confirm that NM-II periodic distribution indeed correlates with actin MPS, we performed Triton X-100 extraction before fixation in order to specifically remove the subcortical actin MPS components as previously reported (Zhong et al., 2014). Following this extraction, we observed a significant reduction in actin MPS (Fig. S6, c and d), confirming the disruption of the membrane-associated actin MPS. Together with this reduction, we detected a dramatic reduction in NM-II–positive puncta (Fig. S6 e). This concomitant decrease in both actin MPS and NM-II (Fig. S6 f) further supports the notion that NM-II associates with actin MPS. Together, these results suggest that NM-II activity keeps the subcortical periodic actin rings constitutively contracted.

### Short-term inhibition of NM-II activity causes axon dilation and interferes with the long-range retrograde trafficking of large cargoes

To test whether axon radial contractility has a functional role in cargo transport, we examined the effect of blebbistatin on
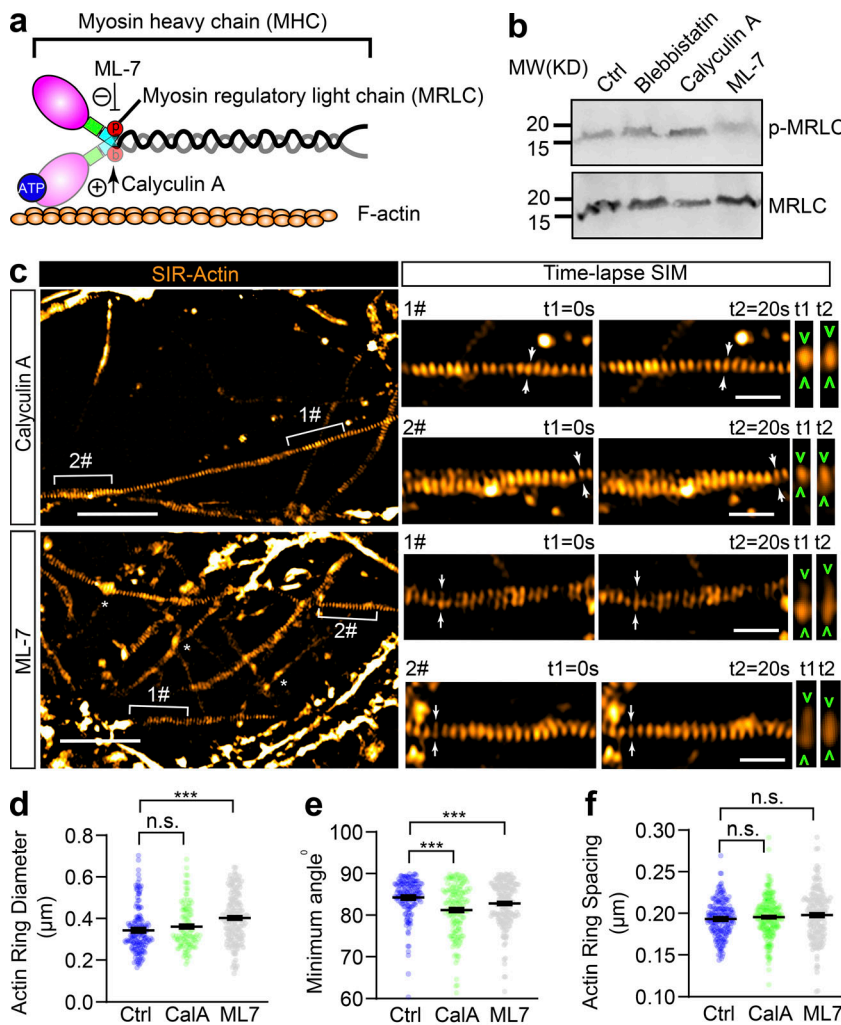
Figure 5. **Inhibition of MRLC phosphorylation slightly affects the diameter and tilting angle of axonal actin rings, but not their periodic spacing.** **(a)** Cartoon showing the organization of actomyosin structure in nonmuscle cells, with the effecting sites of ML-7 and Calyculin A on MRLC annotated. **(b)** Western blot showing the level of diphosphorylated MRLC (p-MRLC) following 30 min treatment with blebbistatin (10 µM), ML-7 (10 µM), and Calyculin A (50 nM). **(c)** In cultured hippocampal neurons, endogenous periodic axonal actin rings were labeled using SiR-actin and live imaged using 2D SIM. Representative time-lapse SIM images of axonal actin rings are shown following 30 min of treatment with ML-7 (10 µM) or Calyculin A (50 nM), respectively. Bracketed regions are magnified in right panels. Dynamic diameter changes of actin rings are annotated with arrowheads. Scale bars = 5 µm (left) and 1 µm (right). **(d–f)** Quantification of the diameter (d), minimum tilting angle (e), and spacing (f) of the periodic actin rings along the axon. Data represent mean ± SEM; $n$ = 167 (control [Ctrl]), 170 (Calyculin A [CalA]), and 175 (ML-7), values are labeled on the panels, representing numbers of axonal actin rings analyzed. Values were measured from three independent cultures (***, P < 0.001, two-tailed unpaired $t$ test). MW, molecular weight; n.s., not significant.

retrograde axonal trafficking in neurons grown in a six-well microfluidic device (Fig. S7 a), where we could restrict the action of blebbistatin to the axon segments by adding it through the middle chamber (Fig. S7 b). Widespread dilation of the axonal diameter (Fig. S7, c and d) and volume (Fig. S7 e) along the longitudinal axis was observed using 3D SIM following 90 min of blebbistatin incubation. To test the integrity of these treated axons, we further examined the axonal microtubule structure by dual-color SIM using a β-tubulin III antibody and phalloidin (Fig. S7 f). We found that neither the microtubule bundle intensity (Fig. S7 g) nor the width (Fig. S7 h) were affected by 60-min blebbistatin treatment. This blebbistatin treatment also failed to affect the mitochondrial anchoring, as the movement of the immobile mitochondrial fraction was not affected (Fig. S7, i and j), whereas the mobile fractions with the higher average speeds were significantly increased by the blebbistatin movement (Fig. S7, i and j), suggesting that the NM-II–dependent axonal contractility is likely to affect the cargo transport.

To further assess the effects of axonal contractility on cargo trafficking, we examined the impact of disrupting NM-II activity on retrograde trafficking in short-term blebbistatin-treated axons. The average speed of CTB-positive carriers before and after blebbistatin treatment for 60 min (Fig. 7 a) were compared. As

demonstrated earlier (Fig. 1 g), small carriers moved faster than large ones in the absence of blebbistatin (Fig. 7 b), whereas blebbistatin treatment specifically increased the trafficking speed of large CTB-positive carriers, but not that of small ones (Fig. 7 b and Video 9). Similarly, an increase of the average speed was observed for large Lysotracker-positive carriers, but not for small ones (Fig. 7 c and Video 10). These results indicate that the short-term relaxation of the axonal actomyosin-II network has an initial positive impact on the trafficking of large cargoes, suggesting that axon radial contractility exerts a local brake on their transport.

Given that the large CTB-positive carrier population showed the most significant increase in speed upon blebbistatin treatment (Fig. 7 b), we chose these carriers for more detailed motion analyses in order to further dissect the impact of radial contractility on axonal transport. We used kymograph and instantaneous speed to analyze the movement of individual CTB carriers. We found that 60-min treatment with blebbistatin decreased the proportion of time that individual carriers spent in the pausing (Fig. 7 d, red lines; quantified in Fig. 7 g) and slow-moving states (instantaneous speed, 0–0.4 µm/s; Fig. 7 e, "slow"). Concomitantly, the ratio of time spent in the fast-moving state (instantaneous speed, 0.4–3.2 µm/s) was significantly increased (Fig. 7 e,
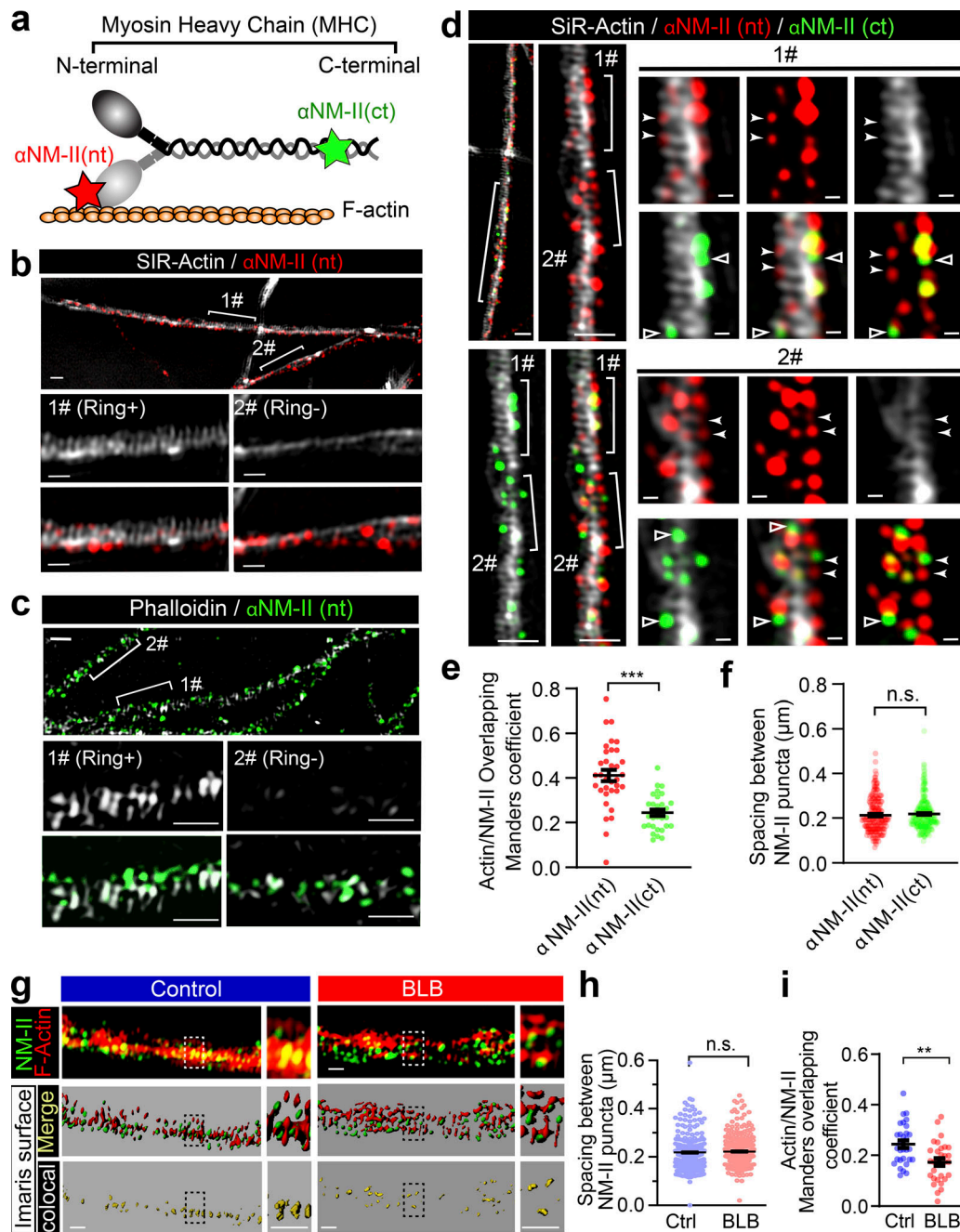
Figure 6. **Periodic actin rings correlate more extensively with the head domain than the rod domain of the NM-II filaments along axons. (a)** Cartoon showing the binding site of antibodies against the NM-II head domain (αNM-II (nt)) and rod domain (αNM-II (ct)), respectively. **(b)** Prior to fixation, DIV14 rat hippocampal neurons were labeled with SiR-actin, fixed and stained for endogenous head domain (αNM-II (nt)), and imaged with dual-color SIM. Bracketed regions with persistent actin rings (Ring+) or without actin rings (Ring−) are magnified in the bottom panels, respectively. Scale bars = 1 μm (top) and 500 nm (bottom). **(c)** Following fixation, DIV14 rat hippocampal neurons were stained for endogenous F-actin (Phalloidin) and head domain (αNM-II (nt)), and imaged with dual-color SIM. Bracketed regions with persistent actin rings (Ring+) or without actin rings (Ring−) are magnified in the bottom panels, respectively. Scale bars = 1 μm (top) and 500 nm (bottom). **(d)** Triple-color SIM image of endogenous F-actin (SiR-actin), head domain (αNM-II (nt)), and rod domain (αNM-II (ct)) of the NM-II along the axon of hippocampal neuron. Bracketed regions are magnified on the right. αNM-II (nt) puncta overlapping with actin rings are annotated with filled arrowheads. αNM-II (ct) puncta not overlapping with actin rings are annotated with hollow arrowheads. Scale bars = 1 μm (left) and 200 nm (right). **(e)** Comparison of colocalization between actin rings with either the head domain (αNM-II (nt)) or the rod domain (αNM-II (ct)) of NM-II filaments. **(f)** Quantification of the spacing between adjacent NM-II puncta in the axonal segments with preserved periodic actin rings. Data represent mean ± SEM; $n$ = 34 (nt) and 33 (ct) axon segments for fraction of the F-actin overlapping with NM-II. **(g)** The NM-II and actin structures resolved with 3D SIM (top) were rendered into surface (middle) using Imaris software; boxed regions are magnified to show the accuracy of the rendering. Colocalization of the bracketed region is shown in the bottom panels. Comparison of colocalization between NM-II and actin rings before and after the 60 min blebbistatin treatment. Scale bars = 0.5 μm. **(h)** Quantification of the spacing between adjacent NM-II puncta in the axonal segments with preserved periodic actin rings in control and blebbistatin-treated neurons. Data represent mean ± SEM; $n$ = 211 (nt) and 285 (ct) in f; $n$ = 262 (ctrl) and 261 (blebbistatin) in i. Values represent numbers of axonal actin rings analyzed. **(i)** The Mander's coefficient reflecting the colocalization rate. b and d are from different ROIs of the same SIM image. Data represent mean ± SEM;

n = 30 (control) and 30 (blebbistatin) axon segments for fraction of the F-actin overlapping with NM-II. Data are from three independent cultures (**, P < 0.01; ***, P < 0.001, two-tailed unpaired t test). n.s., not significant.

"fast"; see also grouped quantification in Fig. 7 f). These results suggest that blebbistatin treatment significantly increased the mobility of these long-range retrograde CTB carriers by increasing the number of fast-moving carriers at the expense of the pausing and slow-moving ones.

We next further investigated the effect of radial contractility on the transport directionality of individual CTB carriers within the microfluidic channels (Fig. 7 a). We noted that their trajectories were predominately composed of two states, (1) a directed state and (2) an undirected state, as indicated by the sloped and the vertical lines, respectively, in the displacement time plot (Fig. 7 h). Following 60-min blebbistatin treatment, the speed of the directed state was significantly increased, as indicated by the flatter slopes (Fig. 7 h), whereas in the undirected state, we observed pronounced back-and-forth motion (Fig. 7 h, asterisks; Video 9), which has been previously described as low-efficiency trafficking pattern for long-range cargo transport (Yi et al., 2011). This is consistent with our observation that the ratio of the fast-moving CTB carriers increases at the expense of slow-moving ones (Fig. 7, e and f; see also Fig. S7 k). To further quantify these back-and-forth movements, we compared the ratio of direction swap (Sr) in these tracks by measuring the ratio of the time cargoes spent traveling in the reverse direction ($t_{rev}$) in relation to the total time traveled ($t_{total}$), as shown in Eq. 1, with k being the number of trajectories:

$$Sr = \frac{\sum_{k=0}^{n} t_{rev}{}^{k}}{\sum_{k=0}^{n} t_{total}{}^{k}}.$$ (1)

This analysis revealed that blebbistatin treatment significantly increased the amount of time cargoes underwent reverse motion, thereby increasing the ratio of direction swap in cargoes moving along the axon (Fig. 7 i). Accordingly, we found that blebbistatin treatment decreased the number of CTB-positive carriers that traversed the imaging window within a given time (Fig. 7 j), suggesting that the overall retrograde trafficking efficiency was reduced. These results support the positive role of axonal radial contractility in maintaining near-unidirectional retrograde trafficking, thereby ensuring the overall efficiency of long-range retrograde transport.
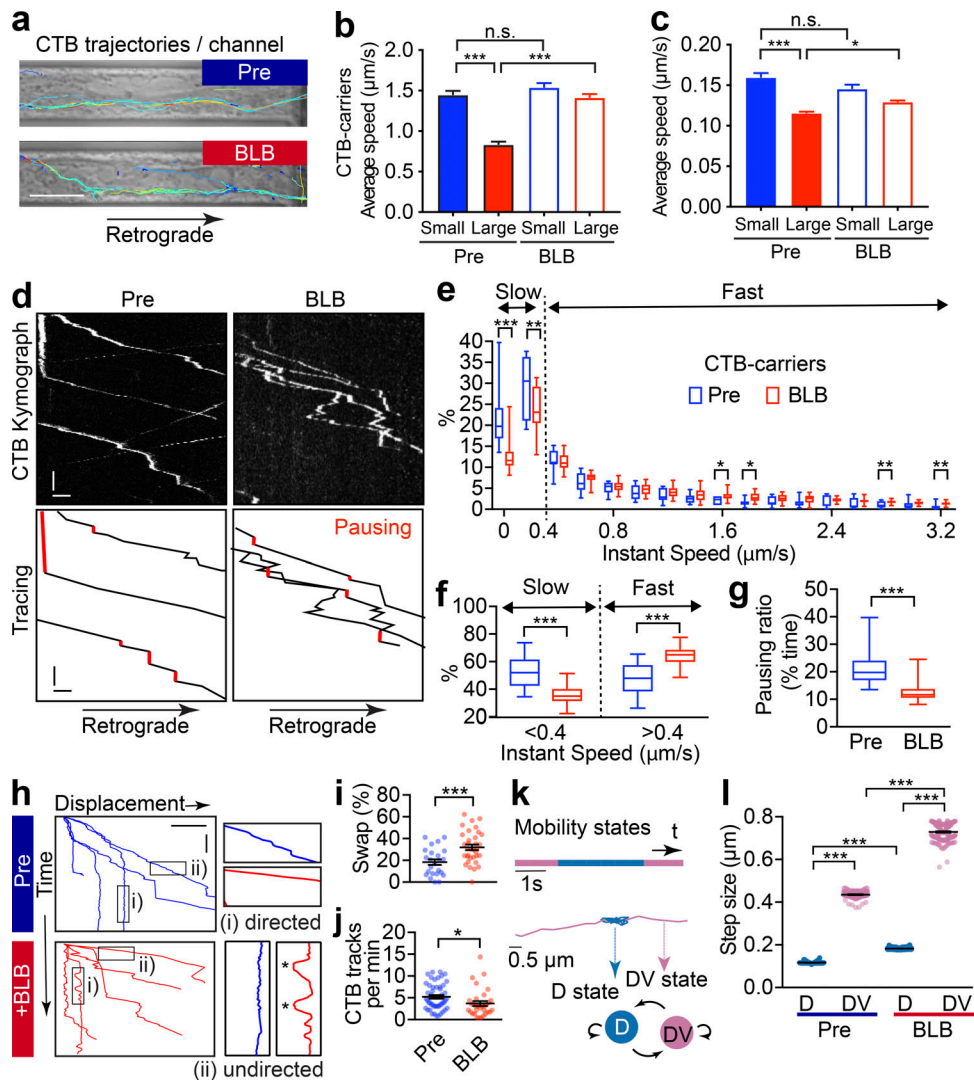
We next investigated how the radial contractility impacted the mobility of directed and undirected carriers, respectively, by analyzing the dynamics of the CTB-positive carrier movements. To objectively and quantitatively analyze the effect of the contractility on the two motion states, we employed a two-state hidden Markov model (HMM) to annotate these CTB trajectories into undirected (D) and directed (DV) states (Fig. 7 k), as previously described (Joensuu et al., 2017). The separating efficacy of this model was demonstrated by the fact that the step sizes of the undirected (0.1168 ± 0.45 μm) and directed transport states (0.4352 ± 1.53 μm) were distinct from each other. We then examined the effect of blebbistatin treatment and found that it significantly increased the step size of large CTB-positive carriers in the DV state (Fig. 7 l, pink spots), which is in good

agreement with our earlier observation of the increased average (Fig. 7 b) and instant speed (Fig. 7, e–g; and Video 9) of CTB carriers following short-term blebbistatin treatment. For the D state in pretreated axons, CTB-positive carriers exhibited a much smaller step size (Fig. 7 l), indicating that the mobility of these undirected carriers was constrained. However, this limited step size was significantly increased following 60-min blebbistatin treatment (Fig. 7 l, blue spots). Taken together, the reduced pausing ratio (Fig. 7 g) and an increased back-and-forth movement (Fig. 7, h and i) suggests that the mobility of the undirected CTB carriers is increased following disruption of NM-II activity by blebbistatin. These results suggest the effect of 60-min blebbistatin treatment significantly increased the speed of both directed- and undirected-moving CTB carriers. Our findings indicate that the axonal actomyosin network maintains radial constriction, which not only impedes the speed of the directed fast-moving state but also suppresses the low-efficiency back-and-forth movement during the undirected state of these long-range carriers. The overall impact of this contractility on long-range trafficking is therefore positive, which facilitates the unidirectionality and the overall efficiency of long-range retrograde carriers.

## Prolonged inactivation of actomyosin-II disrupts the periodic actin rings and causes FAS

We also used genetic approaches to explore the impact of longer-term manipulations of NM-II expression and activity on axonal structural stability. First, we used commercially available pre-designed siRNA constructs against MHC of NM-IIB (siNM-II) to specifically down-regulate the NM-II level in cultured cells. We found the endogenous NM-II level in two different siNM-II transfected cells was significantly reduced (Fig. 8, a–c). We also noticed a significant increase in the formation of FAS along the axons of siNM-II transfected neurons (Fig. 8 b, arrowheads; and Fig. 8 d). We further used SiR-actin to label the periodic actin rings in NM-II knock down neurons and found that the periodic actin rings were largely disrupted, as we detected accumulated actin blobs (Fig. 8 e, arrowheads; and Fig. 8 f) and black patches devoid of actin (Fig. 8 e, brackets). As disassembly of actin MPS is one of the earliest steps underlying axon degeneration (Unsain et al., 2018; Wang et al., 2019), and FAS is a hallmark of irreversible axonal damage (Maia et al., 2015), our results suggested that disrupting axonal radial contractility could disturb the axonal MPS, leading to FAS and subsequent degeneration.

Next, in addition to siRNA knockdown of endogenous NM-II, we also manipulated the NM-II activity by transfecting cultured neurons with the MRLC mutants, including S19AT18A (AA) or S19AT18A (DD) mutations, which abolish or enhance the NM-II activity (Beach et al., 2011), respectively. We found that 48 h after NM-II (AA)-GFP transfection, the structural integrity of transfected axons was significantly disrupted, as reflected by the significantly increased diameter fluctuations (Fig. 8, g and i),

Wang et al.
NM-II facilitates axonal trafficking and stability

Journal of Cell Biology    10 of 19
https://doi.org/10.1083/jcb.201902001

Figure 7. **Short-term inactivation of actomyosin-II reduces the efficiency of retrograde axonal trafficking. (a)** DIV14 rat hippocampal neurons were cultured in microfluidic devices, and the axon segments were subjected to short-term blebbistatin treatment (10 μM, 60 min). Trajectories of CTB-positive cargoes in the axon channels were traced before (pre) and after (+BLB) blebbistatin treatment. Scale bar = 10 μm. **(b and c)** Track speed (trajectory length/duration) of the CTB carriers (b) or Lysotracker carriers (c) before (pre) and after (+BLB) blebbistatin treatment. The speeds of these carriers were subgrouped according to their diameters. Data represent mean ± SEM; n = 248, 287, 271, and 286 (CTB) and n = 179, 342, 128, and 573 (Lysotracker) trajectories from three independent cultures (*, P < 0.05, ***; P < 0.001, two-tailed unpaired t test). The same data of pretreated groups were used in Fig. 1 g and Fig. S1, b–d. **(d)** Representative kymographs of CTB carriers in single axons before (Pre) and after 60-min blebbistatin (+BLB) treatment. Tracings of retrograde CTB carriers are shown in the right panels. Pausing states with the trajectories are indicated with red. x bar = 5 s; y bar = 1 μm. **(e)** Frequency distribution of the instant speed of CTB carriers. Showing a significant decrease in the frequency of slow carriers (0–0.4 μm/s) and a significant increase in the fast carriers (0.4–3.2 μm/s). **(f)** Grouped analysis of instant speeds of slow or fast CTB carriers showing a significant difference before (Pre) and after 60-min blebbistatin (+BLB) treatment. **(g)** The ratio of pausing CTB carriers (instant speed, 0–0.2 μm/s). Data are shown in box and whiskers (min to max); n = 11 (Pre) and 19 (+BLB) axon channels from three independent preparations (*, P < 0.05; **, P < 0.01; ***, P < 0.001, two-tailed unpaired t test; e–g). **(h)** Displacement–time plot of representative Imaris-traced CTB trajectories. Directed (i) and undirected (ii) states, as magnified on the right, with the back-and-forth movements marked with asterisks. x bar = 10 μm; y bar= 20 s. **(i)** Time ratio of cargo traveling in the reverse direction (swap) to total time traveled. Data represent mean ± SEM; n = 28 (Pre) and 34 (+BLB) channels from three independent preparations (***, P < 0.001, two-tailed unpaired t test). **(j)** Quantification of the frequency of CTB-labeled vesicles that cross the observation window per minute. Data represent mean ± SEM; n = 51 (Pre) and 32 (+BLB) channels from three independent preparations (*, P < 0.05, two-tailed unpaired t test). **(k)** CTB trajectory displays directed (D, blue) and undirected (DV, pink) motion states inferred by HMM-Bayes analysis. Example of an annotated trajectory color-coded with the indicated motion states. The time line shows the temporal (s) sequence of the inferred D and DV motion states. **(l)** Step sizes of the two motion states before (pre) and after (+BLB) blebbistatin treatment. Data represent mean ± SEM; from left to right, n = 126, 126, 190, and 190 different trajectories from three independent preparations (***, P < 0.001, two-tailed unpaired t test). n.s., not significant.

disrupted SiR-actin–labeled periodic rings (Fig. 8 h), and abnormal accumulation of FAS (Fig. 8 j) compared with those transfected with wild-type (MRLC(WT)-GFP) or constitutive active (MRLC(DD)-GFP) constructs. These results suggest that the long-term inactivation of actomyosin-II impairs the underlying periodic actin rings and causes irreversible structural damage to the axon, which eventually lead to degeneration.
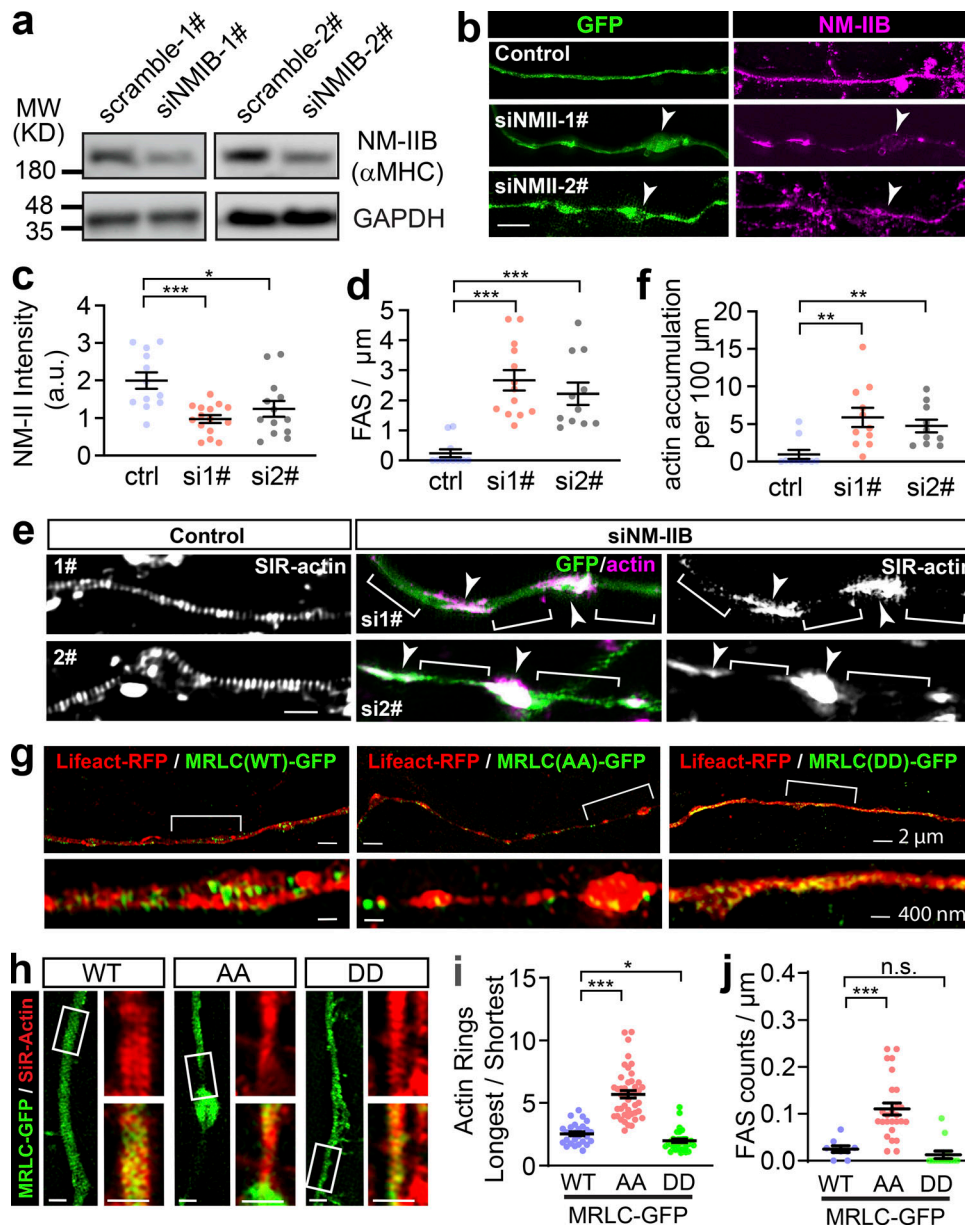
Figure 8. **Long-term down-regulation of actomyosin-II activity disrupts the periodic actin rings and causes the formation of FAS. (a)** Knockdown efficiency of predesigned siRNA constructs. PC12 cells transfected with two different siRNAs targeting MHC of NM-IIB (siNMII-1# and siNMII-2#). Cell lysates were used to detect the endogenous MHC level of NM-IIB by Western blot. **(b)** Representative images of axons in siNMII transfected neurons; arrowheads indicate the FAS. Scale bar = 5 μm. **(c and d)** Quantification of the NM-II fluorescence intensity (c) and FAS number (d) of siNM-II 1# and 2# transfected axons shown in b. **(e)** Representative images showing that along the siNM-II transfected axons, periodic actin structures were disrupted. The unevenly distributed F-actin–accumulation and F-actin–absent black patches are marked with arrowheads and brackets, respectively. Scale bar = 1 μm. **(f)** Quantification of the F-actin accumulation along the siNM-II 1# and 2# axons. **(g)** Rat hippocampal neurons were cotransfected on DIV12 with the Lifeact-mRFP and either MRLC (WT)-GFP, S19AT18A (MRLC (AA)-GFP), or S19DT18D (MRLC (DD)-GFP) plasmids. **(h)** SiR-actin labeling shows disrupted periodicity of actin rings in MRLC(AA)-GFP, but not (WT), (DD)-GFP transfected axons, respectively. Scale bars = 1 μm. **(i and j)** The actin ring diameter fluctuations (i) and the FAS numbers per μm (j) of transfected axons were quantified. Data represent mean ± SEM; n = 12, 15, and 13 for c; n = 11, 13, and 11 for d; n = 10, 11, and 10 for f; n = 28, 45, and 32 for i; and n = 9, 26, and 13 for j (n representing the number of axons analyzed). Data were from two independent preparations (*, P < 0.05; **, P < 0.01; ***, P < 0.001, two-tailed unpaired t test). MW, molecular weight; n.s., not significant.

## Discussion

Many factors affect long-range axonal cargo trafficking (Che et al., 2016; Hancock, 2014; Kapitein and Hoogenraad, 2011; Vale et al., 1992). Nevertheless, the impact of the narrow and rigid axonal plasma membrane on the transiting cargoes remains largely elusive. In this study, we have revealed a novel critical role of axonal NM-II that, by associating with subcortical MPS in the axon shaft, provides subcellular radial constriction that minimizes the axonal swelling and undirected cargo movements. It therefore ensures structural stability as well as cargo-trafficking efficiency along the small-caliber axons.

Wang et al.
NM-II facilitates axonal trafficking and stability

Journal of Cell Biology    12 of 19
https://doi.org/10.1083/jcb.201902001

## Radial contractility facilitates the overall efficiency of long-range retrograde axonal trafficking

An efficient long-range retrograde cargo transport machinery is critical for the survival and function of neurons (Barford et al., 2017; Bilsland et al., 2010; Tojima and Kamiguchi, 2015). The retrograde directionality of the fast-moving cargoes is driven by the progressive minus-end–directed dynein steps, the directionality of which is dependent on the opposing forces they receive (Gennerich et al., 2007). Actomyosin-II controls radial contractility, which poses a steric hindrance to the passaging cargoes (Che et al., 2016) and therefore could potentially affect the opposing force to their driven dyneins. Early studies found that disrupting F-actin in axons does not interfere with organelle transport, which continues unabated or at an even faster rate (Morris and Hollenbeck, 1995), suggesting that the axonal F-actin network acts as a physical impediment to cargo transport. In line with this, we found that short-term blebbistatin treatment released subcellular tension, causing an expansion of the axon diameter and specifically increasing the transport speed of large cargoes. Our results therefore confirm that the directed fast-moving state of large cargoes is subjected to a constant impediment from radial axonal constriction. The undirected stalling of retrograde carriers is also likely to be caused either by a balanced tug-of-war between kinesin and dynein (Belyy et al., 2016) or by the transient detachment of dynein-driven carriers from the microtubule tracks (Gennerich et al., 2007), which is known to be regulated by the load of the cargo (Yi et al., 2011) and the tension-dependent tethering of dynein to the microtubule tracks (Cleary et al., 2014). Consistently, we here show that short-term release of the passaging cargo from local tension leads to a transient increase in carriers' mobility. However, such local tension is also beneficial for axonal transport overall, as long-term actomyosin-II inhibition disrupts axonal cargo trafficking and eventually leads to cargo accumulation at multiple FASs. This suggests that constitutive contractility of the axons provides an efficient way to avoid such cargo accumulations in FAS. The trade-off for such beneficial effect seems to lie in the controlled speed of large carriers. Consistently, expanded axonal diameter induced by adducin knockout also lead to disrupted cargo trafficking and axonal degeneration (Leite et al., 2016).

## Radial contractility along the axonal shafts

The diameter of the long and thin axon has long been believed to be uniform. However, with the development of 3D EM reconstruction, diameter fluctuations have been detected along the length of axons in optical nerves (Giacci et al., 2018). Similarly, in live rat brains, axonal diameter fluctuations were revealed with super-resolution microscopy after the conduction of action potentials (Chéreau et al., 2017). Consistent with these in vivo studies, we have used EM, SR-SIM, and bright-field confocal microscopy to reveal that axons indeed undergo dynamic diameter fluctuations in cultured neurons. Using time-lapse SR-SIM to capture the dynamic changes of subdiffractional membrane-associated structures in live axons, we directly visualized the dynamic radial expansion of both the axonal plasma membrane and the periodic actin rings triggered by the

passages of large axonal cargoes. These transient cargo-induced deformations indicate that (1) the axonal plasma membrane exerts a constant tension to restrict its diameter and (2) the underneath periodic actin rings are constitutively constricted and can undergo radial expansion.

Indeed, these notions are in agreement with observations from previous studies. Zhang et al. (2017) have shown that the axon is the most rigid part of the neuron and is under constitutive tension from the ordered periodic longitudinal MPS composed of actin, spectrin, adducin, and associated proteins (Xu et al., 2013). Depletion of adducin, which caps the barbed actin filaments in the periodic rings, causes progressive axonal dilation and degeneration (Leite et al., 2016), whereas the radial contractility remains unaltered, suggesting the existence of an alternative mechanism for axonal contractility. Moreover, axons are capable of sensing mechanical stimuli and rapidly change their diameter within seconds by forming reversible axonal varicosities along their shafts (Gu et al., 2017). Recently, ultrastructure of periodic actin rings has been resolved as braids made of two long, intertwined actin filaments (Vassilopoulos et al., 2019), and NM-II was found to mediate the purse-string contraction of contractile actin rings during cell division (Henson et al., 2017). These new discoveries all point to the existence of regulative subcortical machinery, which might also involve the activity of actomyosin complexes. However, more live-cell studies using super-resolution microscopy correlated with ultrastructural techniques such as platinum-replica EM will be required to further examine how axonal radial contractility is regulated.

### The actomyosin-II complex is the structural basis underlying the axonal radial contractility

p-MRLC was recently found to distribute with a similar periodicity and largely overlap with the actin MPS at the AIS (Berger et al., 2018). Moreover, depolarization rapidly decreased NM-II activity, indicating that this constricting structure is highly dynamic (Berger et al., 2018; Evans et al., 2017). Tropomyosin isoform Tpm 3.1, which activates and promotes the actin binding to NM-II, has recently been found to display a periodic distribution associated with subcortical actin rings in the AIS (Abouelezz et al., 2019b Preprint). In our study, we revealed that the ~200-nm periodic actomyosin-II filaments are closely associated with actin MPS, in an NM-II–activity-dependent manner, suggesting the actomyosin structure indeed controls the contractility of periodic actin rings. However, considering that the length of NM-II filament is ~300 nm (Henson et al., 2017), it is challenging to place it within individual periodic actin ring. To address this issue, we used triple-color SIM labeling to visualize the localization of either MHC head domain or rod domain with actin rings. Our results point to the NM-II head domain rather than the rod domains colocalizing more extensively with periodic actin rings, suggesting that the NM-II filament is likely to slide across adjacent actin rings, therefore supporting an intra-ring model. This notion was further supported by our observation that manipulations of NM-II activity significantly altered the tilting angles of periodic actin rings. Therefore, our results demonstrate that actomyosin periodicity goes far

Wang et al.
NM-II facilitates axonal trafficking and stability

Journal of Cell Biology    13 of 19
https://doi.org/10.1083/jcb.201902001

beyond the AIS and serves as the structural basis for axonal radial contractility.

### Radial contractility maintains the axonal structural stability

FAS has been noted in several neurodegenerative diseases as well in traumatic brain injuries, with the accumulation of organelles and cargoes at the axonal swellings, and the presence of FAS is generally regarded as an early sign of axonal degeneration (Maia et al., 2015). We found that NM-II knockdown and MRLC inactive mutant–expressing axons exhibited FAS, cargo accumulation, and obvious signs of degeneration. FAS was similarly observed in axons of adducin knockout mice (Leite et al., 2016). This strongly suggests that actomyosin-II–dependent radial contractility is critical to maintain the structural stability of the axon. Indeed, activity of NM-II motors is critical for F-actin turnover (Shutova et al., 2012), increasing the nucleation of actin filaments/bundles in vitro (Ideses et al., 2013) and promoting the fiber assembly of contractile ring and stress fiber in live cells (Abouelezz et al., 2019a; Tojkander et al., 2011). Disruption of the actin MPS is one of the earliest signs and likely the causal factor of axon degeneration, which is marked by FAS and fragmentation (Huang et al., 2017; Unsain et al., 2018; Wang et al., 2019). Given these facts, radial contractility is likely to be of great importance not only to ensure the stability of axonal MPS but also to maintain axonal structural integrity. Additional efforts combining live super-resolution imaging with computational and biophysical approaches will be needed to provide more insights into how axonal contractility is coordinated or disrupted under physiological and pathological conditions in CNS axons.

In summary, we have uncovered an inverse correlation between axonal cargo size and trafficking speed, and demonstrated that axons undergo transient deformation caused by the cargo transition in hippocampal axons. We have further identified the periodic structure of actomyosin-II along the axon shaft as the structural basis of axonal radial contractility. We have also characterized its role in facilitating long-range cargo trafficking by restricting inefficient back-and-forth cargo movement during the undirected state. Our data not only identify a novel role for the axonal actomyosin-II network in long-range cargo trafficking but also highlight the importance of axonal membrane contractility in maintaining the stability of actin MPS along the axon.

## Materials and methods

### Antibodies, molecular reagents, and DNA constructs

SiR-actin (CY-SC001; Cytoskeleton), CellMask Deep Red (H32721; Thermo Fisher Scientific), and predesigned siRNAs were purchased from Invitrogen (catalog number 4390771). siNMII-1# (s135202; 5′-GGAUCGCUACUAUUCAGGAtt-3′), siNMII-2# (s135204, 5′-CAACUAUGCAUCAACUACAtt-3′), Scramble-1# (5′-GGGCUGAAUCCGAUAAUCUtt-3′), and Scramble-2# (5′-GCACAUUACUCAAAUACCAtt-3′) were synthesized from Genomeditech Shanghai. p-MRLC (3674; Cell Signaling), MRLC (8505; Cell Signaling), Cell viability Kit (L34973; Thermo Fisher Scientific), Alexa Fluor 555–, and Alexa Fluor 647–conjugated recombinant CTB were obtained from Thermo Fisher

Scientific (#c-34776 and #c-34777). Mouse anti-synaptobrevin-2 (VAMP2) antibody was obtained from Synaptic Systems (104211), the rabbit anti-NM-IIB(ct) polyclonal antibodies were from Sigma-Aldrich (M7939), and mouse anti-NM-IIB(nt) monoclonal was from Santa Cruz (sc-376954). Microspheres with fluorescence in all four channels were purchased from Thermo Fisher Scientific (Tetra-Speck; 7279). Alexa Fluor 647-phalloidin was purchased from Invitrogen (A22287), while the mouse anti-β-tubulin III was from Covance (MMS-435P). IRDye fluorescent secondary antibodies were from LI-COR (925-32211 and 926-32210); Alexa Fluor secondary antibodies were purchased from Life Technologies. The DNA construct encoding Lifeact-GFP was provided by Roland Wedlich Soldner (MPI Biochemistry, Martinsried, Germany), pTagRFP-mito was purchased from Evrogen (FP147), and pmRFP-LC3 was a gift from Tamotsu Yoshimori (Department of Genetics, Osaka University, Osaka, Japan; plasmid 21075; Addgene). Lysotracker Red DND 99 (7528; Thermo Fisher Scientific). The remaining reagents were obtained from Electron Microscopy Sciences or Sigma-Aldrich unless otherwise specified.

### Neuronal cultures

Hippocampal neurons were cultured from embryonic day 18 embryos from Sprague Dawley rats. All experiments were approved by The University of Queensland Animal Ethics Committee. Hippocampal neurons were prepared as described previously (Wang et al., 2015) and plated on glass coverslips (for confocal microscopy), plastic dishes (for EM), or in microfluidic chambers (RD450; Xona) according to the manufacturer's protocol (Taylor et al., 2005). Hippocampal neurons were transfected between DIV7 and DIV14 with Lipofectamine 2000 (11668019; Thermo Fisher Scientific); briefly, Lipofectamine and DNA/RNA were used in 1:1 ratio and then added into cultured neurons and incubated in serum-free neurobasal medium for >4 h before return to conditioned culture medium. For the pretreated groups, live imaging of approximately five (30 × 12 μm) regions of interest (ROIs) was performed 2 h after the CTB labeling. For blebbistatin treatment, conditioned culture medium containing blebbistatin (10 μM) was only added to the middle and/or terminal chambers of the six-well or four-well microfluidic chambers (TCND500 or RD450; Xona) to exclude its effect on the soma. For the short-term blebbistatin treatment, microfluidic devices were immediately returned to the 37°C imaging chamber for live imaging, and approximately five ROIs were imaged within a total duration of 60 min. For long-term blebbistatin treatment, microfluidic devices were returned to a 37°C $CO_2$ incubator for an additional 2 h before continuing the live imaging.

### Confocal microscopy

Stimulation and labeling were performed in DIV14 rat hippocampal neurons cultured in microfluidic chambers. Briefly, the culture medium was removed from all chambers and the neurons were incubated for 5 min at 37°C in labeling buffer (15 mM Hepes, 145 mM NaCl, 5.6 mM KCl, 2.2 mM $CaCl_2$, 0.5 mM $MgCl_2$, 5.6 mM D-glucose, 0.5 mM ascorbic acid, and 0.1% BSA, pH 7.4), with 50 ng/ml CTB-Af555 or CTB-Af647 added to the nerve terminal chambers only. For Lysotracker labeling, the incubation time

was 30 min. Neurons were then washed three times with warm neurobasal medium and returned to the original conditioned growth medium for 2 h before imaging. Images were acquired with a Zeiss LSM710 inverted microscope maintained at 37°C and 5% $CO_2$, and videos were analyzed for carrier kinetics using the spot function of Imaris software (Imaris7.7-9.2; Bitplane). Kymographs were generated using ImageJ software (National Institutes of Health) using the plugin Multi-Kymograph for ImageJ. For immunofluorescence microscopy of fixed cells, the microfluidic devices were removed and neurons were subsequently fixed for 2–4 h at 4°C with PBS containing 4% PFA and 4% sucrose, followed by immunostaining with indicated antibodies. Permeabilization was performed using 0.1% saponin, 0.2% gelatin, and 1% BSA in PBS for 10 min at 25°C. Imaging was performed on a Zeiss LSM710 Inverted point-scanning laser confocal microscope with spectral detection and high-sensitivity BiG (GaAsP) detectors, using 63× 1.4 NA/190 µm WD/0.132 µm/pixel (1,024 × 1,024) objective in 37°C (live) or 25°C (fixed). Imaging medium was Neurobasal minus phenol red (12348017; Thermo Fisher Scientific). Time-lapse images were analyzed with ZEN 2.1 (Black) version 11.0 and ImageJ software. All images were compiled using Illustrator CS 5.1 (Adobe).

## Imaris tracing of axonal cargoes

Time-lapse videos of CTB-positive or Lysotracker-positive carriers were analyzed for carrier kinetics using the spot function of Imaris software (Imaris7.7-9.2; Bitplane). In brief, region growth was enabled (threshold 50, diameter from border mode), estimated diameter 0.75 µm, tracing with autogressive motion (max distance 2 µm, max gap size 0). Resulted trajectories were filtered with duration >10 s and instant speed >0.07 µm/s. Average speed are calculated as track length divided by track duration. For Lysotracker-positive carriers that bleach rapidly, only the diameter of the first time point in each trajectory was used as the diameter for size grouping.

## Colabeling of F-actin and NM-II for SIM imaging

Cultured rat hippocampal neurons were fixed at DIV14. For dual-color imaging using Phalloidin and NM-II, the fixation protocol was modified from that previously established for maintaining actin ultrastructure (Xu et al., 2013). Briefly, the samples were initially fixed in 4% PFA dissolved in cytoskeleton buffer (CB; 10 mM MES, 150 mM NaCl, 5 mM EGTA, 5 mM glucose, and 5 mM $MgCl_2$, pH 6.1) for 30 min at room temperature and then blocked with antibody dilution buffer (2% BSA with 0.1% Triton X-100 in PBS) for 1 h at room temperature, after which the primary antibody (NM-IIB, diluted 1 in 500) and phalloidin-Af647 (0.14 µM) in 2% BSA in PBS were applied to the dish and incubated at 4°C overnight. Donkey anti-rabbit secondary antibody (A-21206; Thermo Fisher Scientific) was diluted at 1/500 and incubated for 1 h at room temperature. Samples were immediately mounted in Vectashield medium (H-1000; Vector Laboratories) for SIM imaging. For the Triton X-100 extraction experiment, neurons were first treated with the extraction buffer (4% PFA, 0.1% [vol/vol] Triton X-100, and 1 µg/ml phalloidin in CB) for 45 s before the fixation and staining steps. For labeling of live neurons using SiR-actin, newly dissolved SiR-actin was added to culture medium at dilution rate of 1/1,000, followed by incubation for 2 h at 37°C. These neurons in glass-bottom dishes were then washed once with warm phenol-red free Neurobasal medium before imaging using a Zeiss ELYRA PS.1 SR-SIM system at 30°C.

## SIM

Imaging of live and fixed specimens was performed using an Alpha Plan-Apochromat 100×/1.46 NA oil-immersion objective on a Zeiss ELYRA PS.1 SIM/PALM/STORM (SIM/photo-activated localization microscopy/stochastic optical reconstruction microscopy) super-resolution microscope (Carl Zeiss) built around an inverted Axio Observer.Z1 body and equipped with an sCMOS camera (PCO AG) for SIM acquisition and an iXon Ultra 897 electron multiplying charge-coupled device camera (Andor Technology) for PALM/STORM and controlled using ZEN 2.1 (Black) version 11.0. For live imaging of the SiR-actin labeled neurons, images were obtained with the Fastframe mode (100-ms exposure time, a time series of 200 frames at 20-s intervals, a SIM grating size of 51 µm at 640-nm excitation and using five rotations). For fixed and stained samples, images were obtained by acquiring z stacks of 10–16 slices with a spacing of 0.101 µm, an exposure time of 100 ms, a SIM grating size of 42–51 µm at 488-nm and 561-nm excitation and using five rotations. 3D structured illumination images were then reconstructed from the raw SIM data and channel alignment performed using Zen software. To ensure proper alignment of all channels, four-channel SIM data were acquired and processed using 100-nm multi-spectral beads mounted on a calibration slide (1783–455; Carl Zeiss) and channel alignment performed within Zen using the method Affine to provide a stretch and rotation dimension to the alignment, and the resulting data table was saved in a BIN file to be applied on multichannel specimen data. For cross-correlation analysis, line profiles were selected based on the standard of the existence of at least four consecutive NM-II peaks in a single axon shaft. The intensity profiles of each of the channels were then obtained using the Multichannel plot profile function of BAR collection (Ferreria et al., 2015) in ImageJ software (National Institutes of Health). The autocorrelation or cross-correlation rate between the different channels was then examined using the xcorr function of MATLAB. The correlation values for each axon segment were averaged and plotted. Mander's colocalization coefficient (Manders et al., 1993), $M_{Actin/NM-II}$, is described by Eq. 2, using the ImageJ plugin JACoP (Bolte and Cordelières, 2006):

$$M_{Actin/NMII} = \frac{\sum_i (G_{i,coloc})}{\sum_i (G_i)}, \qquad (2)$$

where $G_i$ refers to the intensity values of the actin channels of pixel $i$ and $G_{i,\,coloc}$ is the pixel colocalized with NM-II channel, and where $i$ refers to the $i^{th}$ analyzed pixel of the total image.

## Western blotting

Transfected PC12 cells were lysed with 2× SDS loading buffer and homogenized with syringe and needle. The homogenate was boiled in 95°C for 5 min, fractionated by SDS-PAGE, and then transferred to a polyvinylidene difluoride membrane. After

Wang et al.
NM-II facilitates axonal trafficking and stability

Journal of Cell Biology   15 of 19
https://doi.org/10.1083/jcb.201902001

blocking with Odyssey TBS blocking buffer for 30 min, membranes were washed once with TBST (1× TBS and 0.1% Tween 20 detergent) and incubate with antibodies against MRLC (1:1,000), p-MRLC (1:1,000), MHC (1:1,000), GAPDH (1:5,000), or β-actin (1:5,000) at 4°C overnight. Membranes were then washed three times with TBST and incubated with 1:20,000 dilution of fluorescently tagged anti-mouse or anti-rabbit antibodies covered with foil for 1 h. Blots were washed three times with TBST and imaged with Odyssey imaging system according to the manufacturer's protocols.

### Assessment of actin MPS and NM-II abundance
MPSs were defined as the axonal regions with at least four consecutive actin or NM-II peaks along the longitudinal direction. 5–7 of 5 µm × 5 µm ROIs were selected along the axons in each 3D SIM image (50 µm × 50 µm). In each ROI, the length of axon with F-actin MPS was measured with ImageJ by a trained observer blind to the treatment conditions. In the same ROI, the particle number of NM-II staining was also automatically quantified with the Analyze Particle plugin of FIJI. MPS or NM-II abundance was then calculated as the percentage of segment length with an MPS or particle number over the total length of axons in the ROI, respectively.

### EM
Rat hippocampal neurons cultured in microfluidic devices (DIV14–DIV17) were treated as described for confocal microscopy (Wang et al., 2016), except that 10 µg/ml CTB-HRP was added to the nerve terminal chambers for the period of stimulation. Cells were returned to growth medium for 4 h before fixation. All cells were fixed in 2.5% glutaraldehyde for 24 h. Following fixation, they were processed for 3,3′-DAB cytochemistry using the standard protocol. Fixed cells were contrasted with 1% osmium tetroxide and 4% uranyl acetate before dehydration and embedding in LX-112 resin (Harper et al., 2011). Sections (~50 nm) were cut using an ultramicrotome (UC64; Leica). To quantify CTB-HRP endocytosis, presynaptic regions were visualized at 60,000× using a transmission electron microscope (model 1011; JEOL) equipped with a Morada cooled charge-coupled device camera and the iTEM AnalySIS software. Membrane-bound compartments within the cell soma proximal region of the microfluidic channel were analyzed, and the axon diameter measured using ImageJ software.

### HMM-Bayes analysis
HMM was used to predict the particle hidden states and state transition probabilities from experimental trajectories. Using Bayesian model selection in the inference process, the simplest mobility model can be selected to describe these trajectories in an objective manner (Persson et al., 2013). We analyzed the trajectories from each cell of interest using HMM-Bayes software (Monnier et al., 2015). A maximum of two hidden states was set to describe the trajectory movements, diffusion motion (D) and active transport state (DV), which were used to describe the undirected state and the directed state, respectively. In our cases, ≥10 channel ROIs were quantified for the control group and the blebbistatin-treated group, with corresponding trajectory numbers being 126 and 190, respectively. The D state with a low apparent diffusion coefficient state represents the immobile unattached movement. The DV state, which could be described by averaged velocity, represents the active transport attached movement. All of the analyses were performed using MATLAB (R2016a; Math Works). The average step sizes of different transport states were calculated from all D-DV models.

### Statistics
We used GraphPad Prism 7 (GraphPad) for statistical analyses. Results are reported as mean ± SEM. For group comparisons, two-tailed nonparametric $t$ tests or paired $t$ tests were executed. P values < 0.05 indicated statistical significance. No statistical methods were used to predetermine sample sizes. Data distribution was assumed to be normal, but this was not formally tested. There was no formal randomization. Data collection and analysis were performed by different operators, who were blind to the conditions of the experiments.

### Online supplemental material
Fig. S1 shows that the speed of Lysotracker-positive cargoes is inversely correlated with their size and supports Fig. 1. Fig. S2 shows the axonal deformation caused by the unlabeled axonal cargoes in Lifeact-GFP–expressing neurons and supports Fig. 3. Fig. S3 shows the effects of NM-II short-term inactivation in actin MPS and supports Fig. 4. Fig. S4 is an extended analysis on the contractility of actin MPS, supplementing Fig. 4. Fig. S5 shows the colocalization between p-MRLC immunostaining and the actin MPS, supporting Fig. 5. Fig. S6 shows the immunostaining of NM-II filaments and that of periodic actin rings, supplementing Fig. 6. Fig. S7 shows the inactivation of NM-II caused axon diameter expansion without affecting the microtubule structure or docking mitochondria, supplementing Fig. 7. The time-lapse images of axonal trafficking of CTB and Lysotracker in microfluidic devices are shown in Videos 1 and 2. Time-lapse SIM showing the organelle-induced axonal expansions is shown in Video 3. Videos 4 and 5 show the cargo-induced plasma membrane deformation along the axon. Videos 6 and 7 show the cargo-induced periodic actin ring expansion along the axon. Video 8 shows the contractility of the periodic actin rings along the axon. Time-lapse images of axonal trafficking of CTB and Lysotracker in microfluidic devices perfused with Blebbistatin are shown in Videos 9 and 10.

## References

Abouelezz, A., D. Micinski, A. Lipponen, and P. Hotulainen. 2019a. Submembranous actin rings in the axon initial segment are resistant to the action of latrunculin. *Biol. Chem.* 400:1141–1146. https://doi.org/10.1515/hsz-2019-0111

Abouelezz, A., H. Stefen, M. Segerstråle, D. Micinski, R. Minkeviciene, E.C. Hardeman, P.W. Gunning, C.C. Hoogenraad, T. Taira, T. Fath, and P. Hotulainen. 2019b. Tropomyosin Tpm3.1 is required to maintain the structure and function of the axon initial segment. *bioRxiv.* doi:10.1101/711614 (Preprint posted August 27, 2019).

Altick, A.L., L.M. Baryshnikova, T.Q. Vu, and C.S. von Bartheld. 2009. Quantitative analysis of multivesicular bodies (MVBs) in the hypoglossal nerve: evidence that neurotrophic factors do not use MVBs for retrograde axonal transport. *J. Comp. Neurol.* 514:641–657. https://doi.org/10.1002/cne.22047

Arnold, D.B., and G. Gallo. 2014. Structure meets function: actin filaments and myosin motors in the axon. *J. Neurochem.* 129:213–220. https://doi.org/10.1111/jnc.12503

Barford, K., C. Deppmann, and B. Winckler. 2017. The neurotrophin receptor signaling endosome: Where trafficking meets signaling. *Dev. Neurobiol.* 77:405–418. https://doi.org/10.1002/dneu.22427

Beach, J.R., L.S. Licate, J.F. Crish, and T.T. Egelhoff. 2011. Analysis of the role of Ser1/Ser2/Thr9 phosphorylation on myosin II assembly and function in live cells. *BMC Cell Biol.* 12:52. https://doi.org/10.1186/1471-2121-12-52

Belyy, V., M.A. Schlager, H. Foster, A.E. Reimer, A.P. Carter, and A. Yildiz. 2016. The mammalian dynein-dynactin complex is a strong opponent to kinesin in a tug-of-war competition. *Nat. Cell Biol.* 18:1018–1024. https://doi.org/10.1038/ncb3393

Berger, S.L., A. Leo-Macias, S. Yuen, L. Khatri, S. Pfennig, Y. Zhang, E. Agullo-Pascual, G. Caillol, M.S. Zhu, E. Rothenberg, et al. 2018. Localized Myosin II Activity Regulates Assembly and Plasticity of the Axon Initial Segment. *Neuron.* 97:555–570.e6. https://doi.org/10.1016/j.neuron.2017.12.039

Bilsland, L.G., E. Sahai, G. Kelly, M. Golding, L. Greensmith, and G. Schiavo. 2010. Deficits in axonal transport precede ALS symptoms in vivo. *Proc. Natl. Acad. Sci. USA.* 107:20523–20528. https://doi.org/10.1073/pnas.1006869107

Bolte, S., and F.P. Cordelières. 2006. A guided tour into subcellular colocalization analysis in light microscopy. *J. Microsc.* 224:213–232. https://doi.org/10.1111/j.1365-2818.2006.01706.x

Bryce, N.S., G. Schevzov, V. Ferguson, J.M. Percival, J.J. Lin, F. Matsumura, J.R. Bamburg, P.L. Jeffrey, E.C. Hardeman, P. Gunning, and R.P. Weinberger. 2003. Specification of actin filament function and molecular composition by tropomyosin isoforms. *Mol. Biol. Cell.* 14:1002–1016. https://doi.org/10.1091/mbc.e02-04-0244

Che, D.L., P.D. Chowdary, and B. Cui. 2016. A close look at axonal transport: Cargos slow down when crossing stationary organelles. *Neurosci. Lett.* 610:110–116. https://doi.org/10.1016/j.neulet.2015.10.066

Chéreau, R., G.E. Saraceno, J. Angibaud, D. Cattaert, and U.V. Nägerl. 2017. Superresolution imaging reveals activity-dependent plasticity of axon morphology linked to changes in action potential conduction velocity. *Proc. Natl. Acad. Sci. USA.* 114:1401–1406. https://doi.org/10.1073/pnas.1607541114

Chowdary, P.D., D.L. Che, K. Zhang, and B. Cui. 2015. Retrograde NGF axonal transport--motor coordination in the unidirectional motility regime. *Biophys. J.* 108:2691–2703. https://doi.org/10.1016/j.bpj.2015.04.036

Cleary, F.B., M.A. Dewitt, T. Bilyard, Z.M. Htet, V. Belyy, D.D. Chan, A.Y. Chang, and A. Yildiz. 2014. Tension on the linker gates the ATP-dependent release of dynein from microtubules. *Nat. Commun.* 5:4587. https://doi.org/10.1038/ncomms5587

Evans, M.D., C. Tufo, A.S. Dumitrescu, and M.S. Grubb. 2017. Myosin II activity is required for structural plasticity at the axon initial segment. *Eur. J. Neurosci.* 46:1751–1757. https://doi.org/10.1111/ejn.13597

Even-Ram, S., A.D. Doyle, M.A. Conti, K. Matsumoto, R.S. Adelstein, and K.M. Yamada. 2007. Myosin IIA regulates cell motility and actomyosin-microtubule crosstalk. *Nat. Cell Biol.* 9:299–309. https://doi.org/10.1038/ncb1540

Fan, A., A. Tofangchi, M. Kandel, G. Popescu, and T. Saif. 2017. Coupled circumferential and axial tension driven by actin and myosin influences in vivo axon diameter. *Sci. Rep.* 7:14188. https://doi.org/10.1038/s41598-017-13830-1

Ferreria, T., K. Miura, B. Chef, and J. Eglinger. 2015. Scripts: BAR 1.1.6. https://zenodo.org/record/28838#.XlgZuahKiUk https://doi.org/10.5281/zenodo.28838

Ganguly, A., Y. Tang, L. Wang, K. Ladt, J. Loi, B. Dargent, C. Leterrier, and S. Roy. 2015. A dynamic formin-dependent deep F-actin network in axons. *J. Cell Biol.* 210:401–417. https://doi.org/10.1083/jcb.201506110

Gateva, G., E. Kremneva, T. Reindl, T. Kotila, K. Kogan, L. Gressin, P.W. Gunning, D.J. Manstein, A. Michelot, and P. Lappalainen. 2017. Tropomyosin Isoforms Specify Functionally Distinct Actin Filament Populations In Vitro. *Curr. Biol.* 27:705–713. https://doi.org/10.1016/j.cub.2017.01.018

Gennerich, A., A.P. Carter, S.L. Reck-Peterson, and R.D. Vale. 2007. Force-induced bidirectional stepping of cytoplasmic dynein. *Cell.* 131:952–965. https://doi.org/10.1016/j.cell.2007.10.016

Giacci, M.K., C.A. Bartlett, M. Huynh, M.R. Kilburn, S.A. Dunlop, and M. Fitzgerald. 2018. Three dimensional electron microscopy reveals changing axonal and myelin morphology along normal and partially injured optic nerves. *Sci. Rep.* 8:3979. https://doi.org/10.1038/s41598-018-22361-2

Gormal, R.S., T.H. Nguyen, S. Martin, A. Papadopulos, and F.A. Meunier. 2015. An acto-myosin II constricting ring initiates the fission of activity-dependent bulk endosomes in neurosecretory cells. *J. Neurosci.* 35:1380–1389. https://doi.org/10.1523/JNEUROSCI.3228-14.2015

Gu, Y., P. Jukkola, Q. Wang, T. Esparza, Y. Zhao, D. Brody, and C. Gu. 2017. Polarity of varicosity initiation in central neuron mechanosensation. *J. Cell Biol.* 216:2179–2199. https://doi.org/10.1083/jcb.201606065

Ha, J., K.W. Lo, K.R. Myers, T.M. Carr, M.K. Humsi, B.A. Rasoul, R.A. Segal, and K.K. Pfister. 2008. A neuron-specific cytoplasmic dynein isoform preferentially transports TrkB signaling endosomes. *J. Cell Biol.* 181:1027–1039. https://doi.org/10.1083/jcb.200803150

Han, B., R. Zhou, C. Xia, and X. Zhuang. 2017. Structural organization of the actin-spectrin-based membrane skeleton in dendrites and soma of neurons. *Proc. Natl. Acad. Sci. USA.* 114:E6678–E6685. https://doi.org/10.1073/pnas.1705043114

Hancock, W.O. 2014. Bidirectional cargo transport: moving beyond tug of war. *Nat. Rev. Mol. Cell Biol.* 15:615–628. https://doi.org/10.1038/nrm3853

Harper, C.B., S. Martin, T.H. Nguyen, S.J. Daniels, N.A. Lavidis, M.R. Popoff, G. Hadzic, A. Mariana, N. Chau, A. McCluskey, et al. 2011. Dynamin inhibition blocks botulinum neurotoxin type A endocytosis in neurons and delays botulism. *J. Biol. Chem.* 286:35966–35976. https://doi.org/10.1074/jbc.M111.283879

He, J., R. Zhou, Z. Wu, M.A. Carrasco, P.T. Kurshan, J.E. Farley, D.J. Simon, G. Wang, B. Han, J. Hao, et al. 2016. Prevalent presence of periodic actin-spectrin-based membrane skeleton in a broad range of neuronal cell types and animal species. *Proc. Natl. Acad. Sci. USA.* 113:6029–6034. https://doi.org/10.1073/pnas.1605707113

Henson, J.H., C.E. Ditzler, A. Germain, P.M. Irwin, E.T. Vogt, S. Yang, X. Wu, and C.B. Shuster. 2017. The ultrastructural organization of actin and

myosin II filaments in the contractile ring: new support for an old model of cytokinesis. *Mol. Biol. Cell.* 28:613–623. https://doi.org/10.1091/mbc.e16-06-0466

Huang, C.Y., C. Zhang, T.S. Ho, J. Oses-Prieto, A.L. Burlingame, J. Lalonde, J.L. Noebels, C. Leterrier, and M.N. Rasband. 2017. αII Spectrin Forms a Periodic Cytoskeleton at the Axon Initial Segment and Is Required for Nervous System Function. *J. Neurosci.* 37:11311–11322. https://doi.org/10.1523/JNEUROSCI.2112-17.2017

Ideses, Y., A. Sonn-Segev, Y. Roichman, and A. Bernheim-Groswasser. 2013. Myosin II does it all: assembly, remodeling, and disassembly of actin networks are governed by myosin II activity. *Soft Matter.* 9:7127–7137. https://doi.org/10.1039/c3sm50309g

Joensuu, M., P. Padmanabhan, N. Durisic, A.T. Bademosi, E. Cooper-Williams, I.C. Morrow, C.B. Harper, W. Jung, R.G. Parton, G.J. Goodhill, et al. 2016. Subdiffractional tracking of internalized molecules reveals heterogeneous motion states of synaptic vesicles. *J. Cell Biol.* 215:277–292. https://doi.org/10.1083/jcb.201604001

Joensuu, M., R. Martínez-Mármol, P. Padmanabhan, N.R. Glass, N. Durisic, M. Pelekanos, M. Mollazade, G. Balistreri, R. Amor, J.J. Cooper-White, et al. 2017. Visualizing endocytic recycling and trafficking in live neurons by subdiffractional tracking of internalized molecules. *Nat. Protoc.* 12:2590–2622. https://doi.org/10.1038/nprot.2017.116

Kapitein, L.C., and C.C. Hoogenraad. 2011. Which way to go? Cytoskeletal organization and polarized transport in neurons. *Mol. Cell. Neurosci.* 46:9–20. https://doi.org/10.1016/j.mcn.2010.08.015

Kato, Y., N. Fusetani, S. Matsunaga, and K. Hashimoto. 1988. Calyculins, potent antitumour metabolites from the marine sponge Discodermia calyx: biological activities. *Drugs Exp. Clin. Res.* 14:723–728.

Kovács, M., J. Tóth, C. Hetényi, A. Málnási-Csizmadia, and J.R. Sellers. 2004. Mechanism of blebbistatin inhibition of myosin II. *J. Biol. Chem.* 279:35557–35563. https://doi.org/10.1074/jbc.M405319200

Leite, S.C., P. Sampaio, V.F. Sousa, J. Nogueira-Rodrigues, R. Pinto-Costa, L.L. Peters, P. Brites, and M.M. Sousa. 2016. The Actin-Binding Protein α-Adducin Is Required for Maintaining Axon Diameter. *Cell Reports.* 15:490–498. https://doi.org/10.1016/j.celrep.2016.03.047

Liewald, D., R. Miller, N. Logothetis, H.J. Wagner, and A. Schüz. 2014. Distribution of axon diameters in cortical white matter: an electron-microscopic study on three human brains and a macaque. *Biol. Cybern.* 108:541–557. https://doi.org/10.1007/s00422-014-0626-2

Lukinavičius, G., K. Umezawa, N. Olivier, A. Honigmann, G. Yang, T. Plass, V. Mueller, L. Reymond, I.R. Corrêa Jr., Z.G. Luo, et al. 2013. A near-infrared fluorophore for live-cell super-resolution microscopy of cellular proteins. *Nat. Chem.* 5:132–139. https://doi.org/10.1038/nchem.1546

Lukinavičius, G., L. Reymond, E. D'Este, A. Masharina, F. Göttfert, H. Ta, A. Güther, M. Fournier, S. Rizzo, H. Waldmann, et al. 2014. Fluorogenic probes for live-cell imaging of the cytoskeleton. *Nat. Methods.* 11:731–733. https://doi.org/10.1038/nmeth.2972

Maia, P.D., M.A. Hemphill, B. Zehnder, C. Zhang, K.K. Parker, and J.N. Kutz. 2015. Diagnostic tools for evaluating the impact of Focal Axonal Swellings arising in neurodegenerative diseases and/or traumatic brain injury. *J. Neurosci. Methods.* 253:233–243. https://doi.org/10.1016/j.jneumeth.2015.06.022

Mallik, R., D. Petrov, S.A. Lex, S.J. King, and S.P. Gross. 2005. Building complexity: an in vitro study of cytoplasmic dynein with in vivo implications. *Curr. Biol.* 15:2075–2085. https://doi.org/10.1016/j.cub.2005.10.039

Manders, E.M.M., F.J. Verbeek, and J.A. Aten. 1993. Measurement of co-localization of objects in dual-colour confocal images. *J. Microsc.* 169:375–382. https://doi.org/10.1111/j.1365-2818.1993.tb03313.x

McBride, H.M., M. Neuspiel, and S. Wasiak. 2006. Mitochondria: more than just a powerhouse. *Curr. Biol.* 16:R551–R560. https://doi.org/10.1016/j.cub.2006.06.054

Mizushima, N., Y. Ohsumi, and T. Yoshimori. 2002. Autophagosome formation in mammalian cells. *Cell Struct. Funct.* 27:421–429. https://doi.org/10.1247/csf.27.421

Monnier, N., Z. Barry, H.Y. Park, K.C. Su, Z. Katz, B.P. English, A. Dey, K. Pan, I.M. Cheeseman, R.H. Singer, and M. Bathe. 2015. Inferring transient particle transport dynamics in live cells. *Nat. Methods.* 12:838–840. https://doi.org/10.1038/nmeth.3483

Morris, R.L., and P.J. Hollenbeck. 1995. Axonal transport of mitochondria along microtubules and F-actin in living vertebrate neurons. *J. Cell Biol.* 131:1315–1326. https://doi.org/10.1083/jcb.131.5.1315

Narayanareddy, B.R., S. Vartiainen, N. Hariri, D.K. O'Dowd, and S.P. Gross. 2014. A biophysical analysis of mitochondrial movement: differences between transport in neuronal cell bodies versus processes. *Traffic.* 15:762–771. https://doi.org/10.1111/tra.12171

Papadopulos, A., G.A. Gomez, S. Martin, J. Jackson, R.S. Gormal, D.J. Keating, A.S. Yap, and F.A. Meunier. 2015. Activity-driven relaxation of the cortical actomyosin II network synchronizes Munc18-1-dependent neurosecretory vesicle docking. *Nat. Commun.* 6:6297. https://doi.org/10.1038/ncomms7297

Perge, J.A., J.E. Niven, E. Mugnaini, V. Balasubramanian, and P. Sterling. 2012. Why do axons differ in caliber? *J. Neurosci.* 32:626–638. https://doi.org/10.1523/JNEUROSCI.4254-11.2012

Persson, F., M. Lindén, C. Unoson, and J. Elf. 2013. Extracting intracellular diffusive states and transition rates from single-molecule tracking data. *Nat. Methods.* 10:265–269. https://doi.org/10.1038/nmeth.2367

Pesaresi, M., R. Soon-Shiong, L. French, D.R. Kaplan, F.D. Miller, and T. Paus. 2015. Axon diameter and axonal transport: In vivo and in vitro effects of androgens. *Neuroimage.* 115:191–201. https://doi.org/10.1016/j.neuroimage.2015.04.048

Qu, Y., I. Hahn, S.E. Webb, S.P. Pearce, and A. Prokop. 2017. Periodic actin structures in neuronal axons are required to maintain microtubules. *Mol. Biol. Cell.* 28:296–308. https://doi.org/10.1091/mbc.e16-10-0727

Rai, A.K., A. Rai, A.J. Ramaiya, R. Jha, and R. Mallik. 2013. Molecular adaptations allow dynein to generate large collective forces inside cells. *Cell.* 152:172–182. https://doi.org/10.1016/j.cell.2012.11.044

Riedl, J., A.H. Crevenna, K. Kessenbrock, J.H. Yu, D. Neukirchen, M. Bista, F. Bradke, D. Jenne, T.A. Holak, Z. Werb, et al. 2008. Lifeact: a versatile marker to visualize F-actin. *Nat. Methods.* 5:605–607. https://doi.org/10.1038/nmeth.1220

Saitoh, M., T. Ishikawa, S. Matsushima, M. Naka, and H. Hidaka. 1987. Selective inhibition of catalytic activity of smooth muscle myosin light chain kinase. *J. Biol. Chem.* 262:7796–7801.

Salbreux, G., G. Charras, and E. Paluch. 2012. Actin cortex mechanics and cellular morphogenesis. *Trends Cell Biol.* 22:536–545. https://doi.org/10.1016/j.tcb.2012.07.001

Shutova, M., C. Yang, J.M. Vasiliev, and T. Svitkina. 2012. Functions of nonmuscle myosin II in assembly of the cellular contractile system. *PLoS One.* 7:e40814. https://doi.org/10.1371/journal.pone.0040814

Tammineni, P., X. Ye, T. Feng, D. Aikal, and Q. Cai. 2017. Impaired retrograde transport of axonal autophagosomes contributes to autophagic stress in Alzheimer's disease neurons. *eLife.* 6:e21776. https://doi.org/10.7554/eLife.21776

Taylor, A.M., M. Blurton-Jones, S.W. Rhee, D.H. Cribbs, C.W. Cotman, and N.L. Jeon. 2005. A microfluidic culture platform for CNS axonal injury, regeneration and transport. *Nat. Methods.* 2:599–605. https://doi.org/10.1038/nmeth777

Tojima, T., and H. Kamiguchi. 2015. Exocytic and endocytic membrane trafficking in axon development. *Dev. Growth Differ.* 57:291–304. https://doi.org/10.1111/dgd.12218

Tojkander, S., G. Gateva, G. Schevzov, P. Hotulainen, P. Naumanen, C. Martin, P.W. Gunning, and P. Lappalainen. 2011. A molecular pathway for myosin II recruitment to stress fibers. *Curr. Biol.* 21:539–550. https://doi.org/10.1016/j.cub.2011.03.007

Unsain, N., M.D. Bordenave, G.F. Martinez, S. Jalil, C. von Bilderling, F.M. Barabas, L.A. Masullo, A.D. Johnstone, P.A. Barker, M. Bisbal, et al. 2018. Remodeling of the Actin/Spectrin Membrane-associated Periodic Skeleton, Growth Cone Collapse and F-Actin Decrease during Axonal Degeneration. *Sci. Rep.* 8:3007. https://doi.org/10.1038/s41598-018-21232-0

Vale, R.D., F. Malik, and D. Brown. 1992. Directional instability of microtubule transport in the presence of kinesin and dynein, two opposite polarity motor proteins. *J. Cell Biol.* 119:1589–1596. https://doi.org/10.1083/jcb.119.6.1589

Vassilopoulos, S., S. Gibaud, A. Jimenez, G. Caillol, and C. Leterrier. 2019. Ultrastructure of the axonal periodic scaffold reveals a braid-like organization of actin rings. *Nat. Commun.* 10:5803. https://doi.org/10.1038/s41467-019-13835-6

Wang, T., S. Martin, A. Papadopulos, C.B. Harper, T.A. Mavlyutov, D. Niranjan, N.R. Glass, J.J. Cooper-White, J.-B. Sibarita, D. Choquet, et al. 2015. Control of autophagosome axonal retrograde flux by presynaptic activity unveiled using botulinum neurotoxin type a. *J. Neurosci.* 35:6179–6194. https://doi.org/10.1523/JNEUROSCI.3757-14.2015

Wang, T., S. Martin, T.H. Nguyen, C.B. Harper, R.S. Gormal, R. Martínez-Mármol, S. Karunanithi, E.J. Coulson, N.R. Glass, J.J. Cooper-White, et al. 2016. Flux of signalling endosomes undergoing axonal retrograde transport is encoded by presynaptic activity and TrkB. *Nat. Commun.* 7:12976. https://doi.org/10.1038/ncomms12976

Wang, G., D.J. Simon, Z. Wu, D.M. Belsky, E. Heller, M.K. O'Rourke, N.T. Hertz, H. Molina, G. Zhong, M. Tessier-Lavigne, and X. Zhuang. 2019. Structural plasticity of actin-spectrin membrane skeleton and functional role of actin and spectrin in axon degeneration. *eLife.* 8:e38730. https://doi.org/10.7554/eLife.38730

Wortman, J.C., U.M. Shrestha, D.M. Barry, M.L. Garcia, S.P. Gross, and C.C. Yu. 2014. Axonal transport: how high microtubule density can compensate for boundary effects in small-caliber axons. *Biophys. J.* 106: 813–823. https://doi.org/10.1016/j.bpj.2013.12.047

Xu, K., G. Zhong, and X. Zhuang. 2013. Actin, spectrin, and associated proteins form a periodic cytoskeletal structure in axons. *Science.* 339: 452–456. https://doi.org/10.1126/science.1232251

Yi, J.Y., K.M. Ori-McKenney, R.J. McKenney, M. Vershinin, S.P. Gross, and R.B. Vallee. 2011. High-resolution imaging reveals indirect coordination of opposite motors and a role for LIS1 in high-load axonal transport. *J. Cell Biol.* 195:193–201. https://doi.org/10.1083/jcb.201104076

Yin, X., G.J. Kidd, N. Ohno, G.A. Perkins, M.H. Ellisman, C. Bastian, S. Brunet, S. Baltan, and B.D. Trapp. 2016. Proteolipid protein-deficient myelin promotes axonal mitochondrial dysfunction via altered metabolic coupling. *J. Cell Biol.* 215:531–542. https://doi.org/10.1083/jcb.201607099

Zhang, Y., K. Abiraman, H. Li, D.M. Pierce, A.V. Tzingounis, and G. Lykotrafitis. 2017. Modeling of the axon membrane skeleton structure and implications for its mechanical properties. *PLOS Comput. Biol.* 13: e1005407. https://doi.org/10.1371/journal.pcbi.1005407

Zhong, G., J. He, R. Zhou, D. Lorenzo, H.P. Babcock, V. Bennett, and X. Zhuang. 2014. Developmental mechanism of the periodic membrane skeleton in axons. *eLife.* 3:e04581. https://doi.org/10.7554/eLife.04581
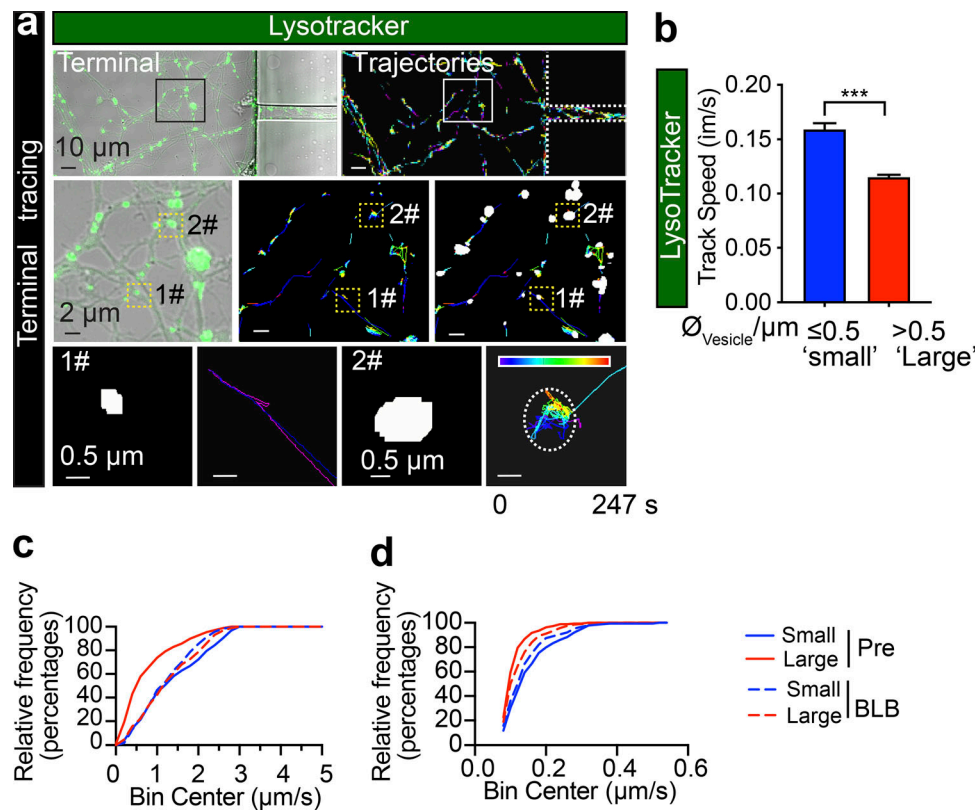
Figure S1. **The speed of Lysotracker-positive cargoes is inversely correlated with their size in axons of cultured hippocampal neurons. (a)** Representative time-lapse images of Lysotracker carriers at the nerve terminals of DIV14 rat hippocampal neurons. Top left: Lysotracker labeling at nerve terminals as isolated by the device. Top right: Imaris tracing trajectories of the same ROI. Trajectories of small (1#, diameter ≤0.5 μm) and large (2#, diameter >0.5 μm) carriers were magnified in the bottom panels, respectively. Rows represent the consecutive zooms of the boxed regions, from row 1 to 3. Panels in the first row, scale bar = 10 μm; second row, scale bar = 2 μm; third row, scale bar = 0.5 μm. **(b)** Grouped analysis of average speeds of Lysotracker-positive cargoes with small ( ≤ 0.5 μm) and large (>0.5 μm) diameters, showing a significant difference. Data represent mean ± SEM from three independent preparations (small, $n =$ 179; big, $n =$ 342 tracks; ***, $P < 0.001$, two-tailed unpaired $t$ test). The same datasets were also used in the pretreated group of Fig. 7 c. **(c)** Cumulative frequency distribution of CTB-positive cargo speed dataset used in Figs. 1 g and 7 b. **(d)** Cumulative frequency distribution of Lysotracker-positive cargo speed dataset used in b and Fig. 7 c.
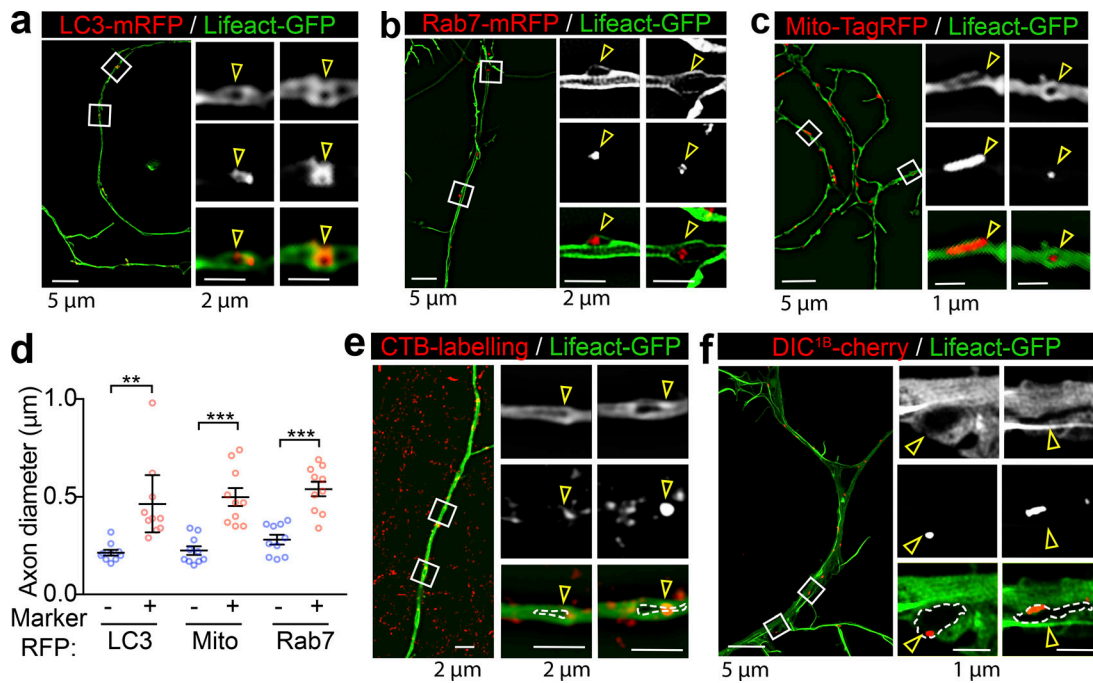
Figure S2. **Large retrograde cargoes produce fluorescence voids within the axons of Lifeact-GFP-expressing neurons. (a–c)** Cultured hippocampal neurons grown in a microfluidic device were transfected on DIV12 with Lifeact-GFP and cotransfected with either LC3-mRFP (autophagosome; a) Rab7-mRFP (late endosome; b), or Mito-TagRFP (mitochondria; c) and subjected to time-lapse imaging on DIV14. Representative dual-color 3D SIM projections of neurons expressing Lifeact-GFP and with different subcellular markers are magnified in the right panels, and overlapping regions are annotated. Scale bars as indicated. **(d)** Quantification of axon diameters with (+) and without (−) annotated markers. Data represent mean ± SEM ($n = 10$ axons for each marker from three independent cultures; **, $P < 0.01$; ***, $P < 0.001$, two-tailed unpaired $t$ test). **(e and f)** Representative dual-color 3D SIM projections of axons expressing Lifeact-GFP, which were colabeled with the retrograde cargo marker CTB (e) or DIC[1B] (f). Boxed regions are magnified in the right panels, and overlapping regions are annotated. Scale bars as indicated. Arrowheads indicate the locations of areas devoid of fluorescence (fluorescent voids).
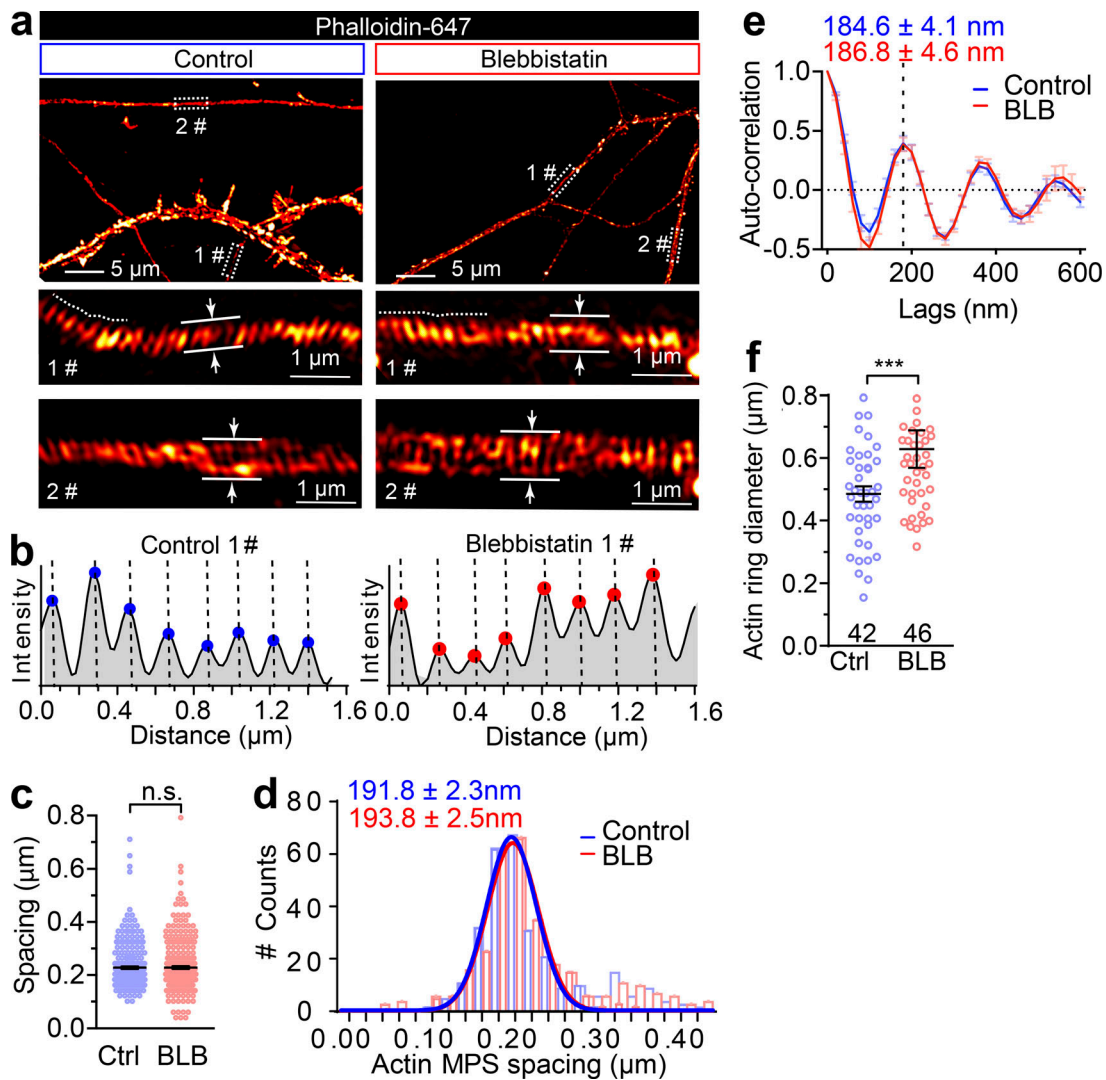
Figure S3. **Short-term inactivation of NM-II increases the axon diameter without affecting the actin ring periodicity. (a)** DIV14 rat axons were stained for endogenous F-actin (phalloidin) and imaged with 3D SIM; two different boxed regions magnified with maximum z-projections shown in the lower panels. Axon diameters were measured as the average of a 1-μm segment. **(b)** Periodic actin peaks were identified using the find peak function of BAR collection in ImageJ (simple moving average = 1), along the line profiles as shown with dashed lines in 1# of panel a. x values of the peaks were extracted (and the distance between adjacent peaks is shown in Fig. 5 f) in both untreated (control) and short-term (60 min) blebbistatin-treated axons. **(c and d)** Comparison of spot plot (c) and Gaussian fitting curve (d) of periodic actin spacing distribution in control and blebbistatin-treated neurons. Data represent mean ± SEM; n = 300 (control) and 316 (blebbistatin treated) for periodicity quantification. **(e)** Autocorrelation analysis of the actin periodicity of control and blebbistatin-treated axons. Data represent mean ± SEM; n = 10 (control) and 8 (blebbistatin-treated) axon segments were measured. **(f)** Quantification of actin diameters in control and blebbistatin-treated axons. Data represent mean ± SEM; n = 42 (control) and 46 (blebbistatin-treated) actin rings diameters were measured. Values were measured from three independent cultures (**, P < 0.05; ***, P < 0.001, two-tailed unpaired t test). n.s., not significant.
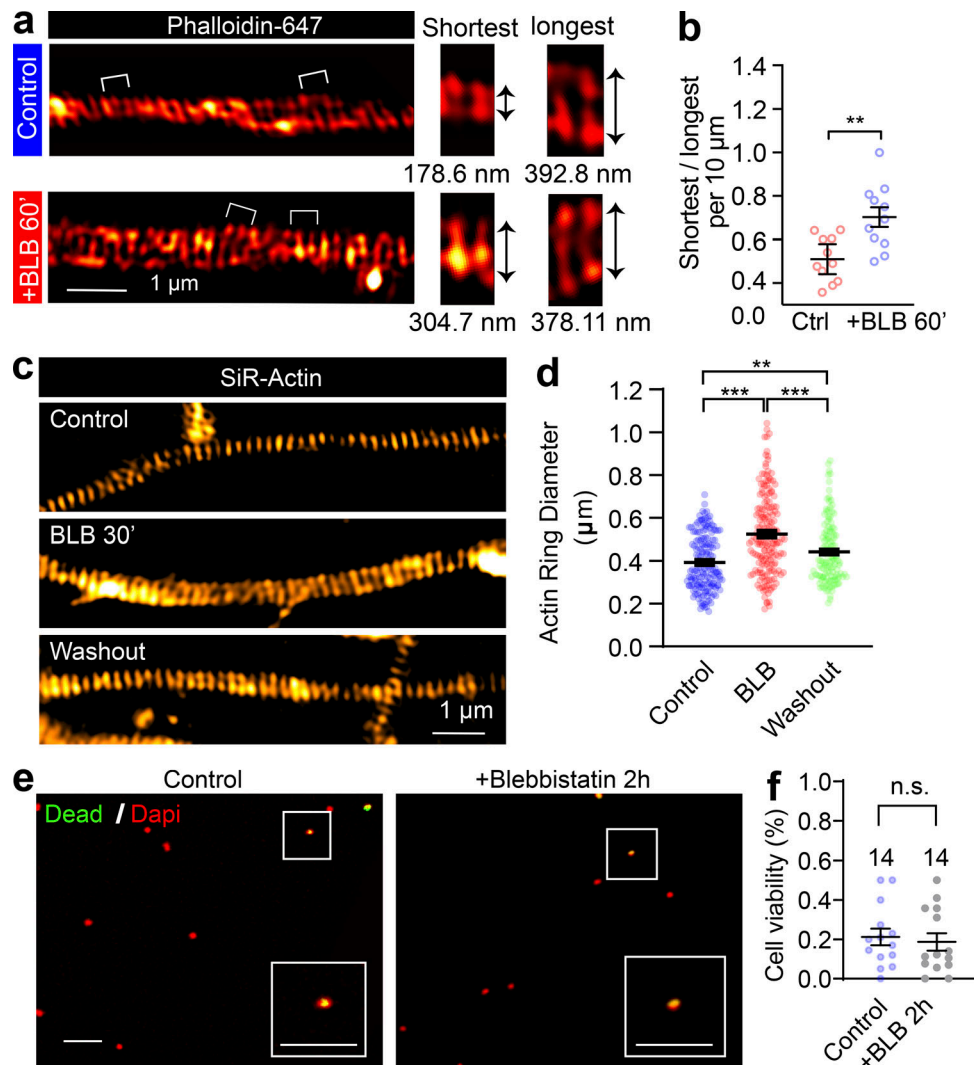
Figure S4. **The effect of blebbistatin on periodic axon actin rings is reversible. (a)** SIM images of endogenous F-actin (phalloidin) along the axon of a DIV14 rat hippocampal neuron before and after short-term blebbistatin treatment (10 µM, 60 min). Bracketed regions are magnified on the right, and the diameters of actin rings are shown below. **(b)** Quantification of actin ring diameter fluctuations; the diameters per 10-µm axon segments were measured and quantified. Data represent mean ± SEM; n = 11 (control) and 11 (blebbistatin-treated) axon segments were analyzed. **(c)** In cultured hippocampal neurons, endogenous periodic axonal actin rings were labeled using SiR-actin and live imaged using SIM. Representative SIM images of axonal actin rings are shown of neurons following DMSO treatment (control), 30-min blebbistatin treatment (BLB), and 12-h incubation after blebbistatin treatment and washout, respectively. Scale bar = 1 µm. **(d)** Quantification of diameters of the periodic actin rings along the axon. **(e)** Viability of neurons treated with 10 µM blebbistatin for 120 min. Boxed regions are amplified in the insets. Scale bars = 50 µm. **(f)** Quantification of viability rate. Data represent mean ± SEM; n values are labeled on the panels, representing numbers of axonal actin rings analyzed. Values were measured from axons of at least three independent cultures (**, P < 0.01; ***, P < 0.001, two-tailed unpaired t test). n.s., not significant.

Wang et al.
NM-II facilitates axonal trafficking and stability

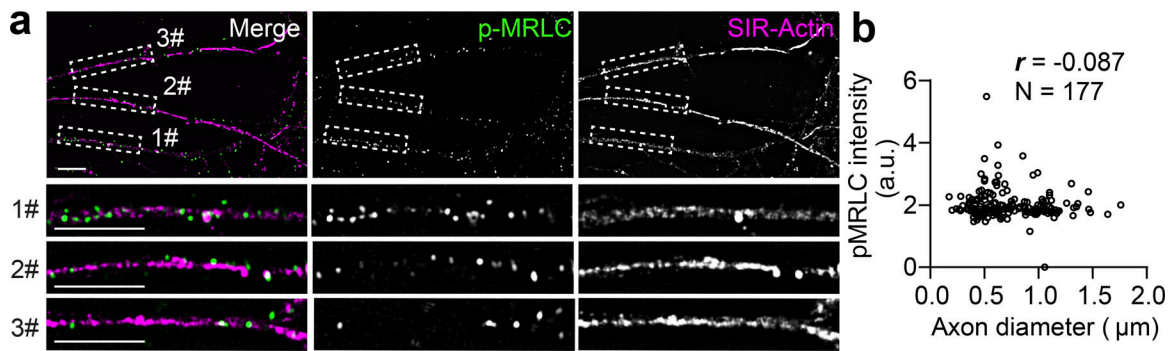**Journal of Cell Biology**    S4
https://doi.org/10.1083/jcb.201902001

**Figure S5.   The phosphorylation of MRLC is not associated with the axonal diameter. (a)** In DIV14 rat hippocampal neurons, endogenous periodic axonal actin rings were labeled using SiR-actin, followed by staining using diphosphorylated MRLC antibody (p-MRLC). Boxed regions are amplified in the bottom panels. Scale bars = 5 µm. **(b)** Pearson's correlation coefficient (*r*) was calculated between the local p-MRLC level and the axon diameter. *n* values are labeled on the panels, representing numbers of axonal segments analyzed. Values were measured from axons of three independent cultures.
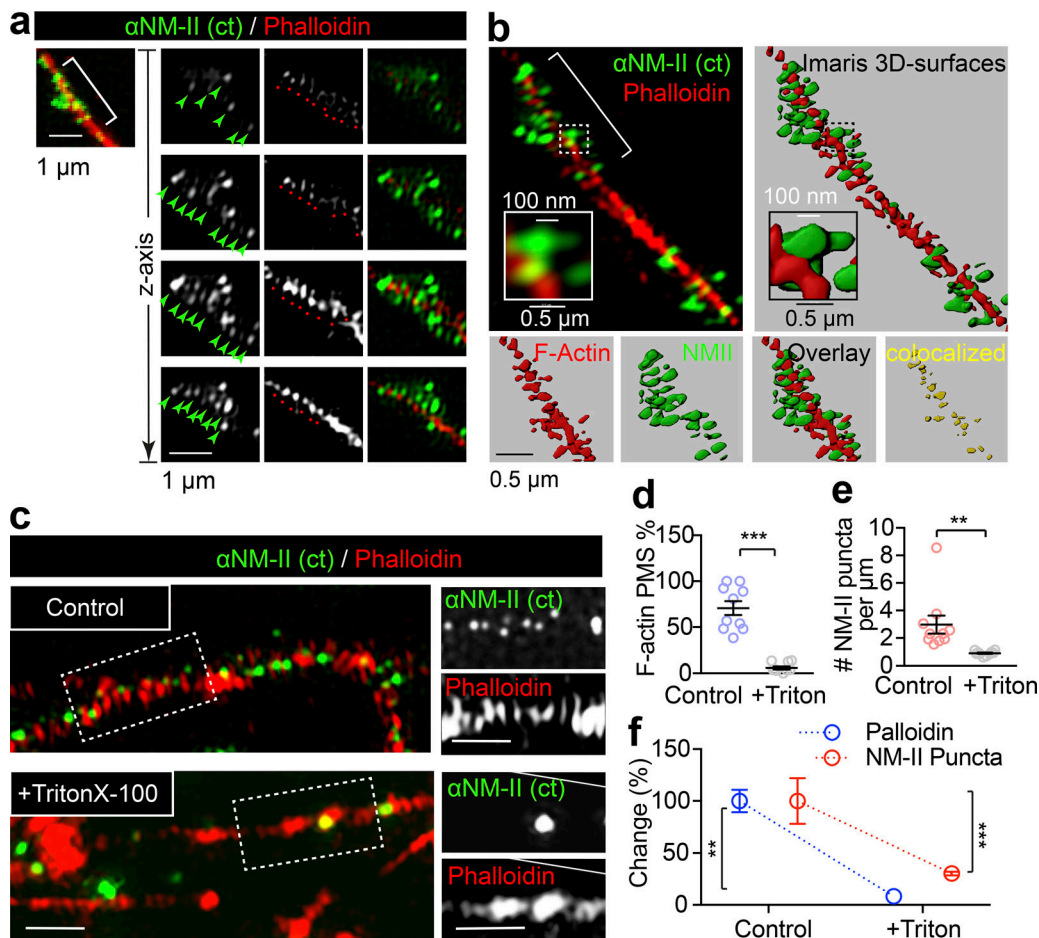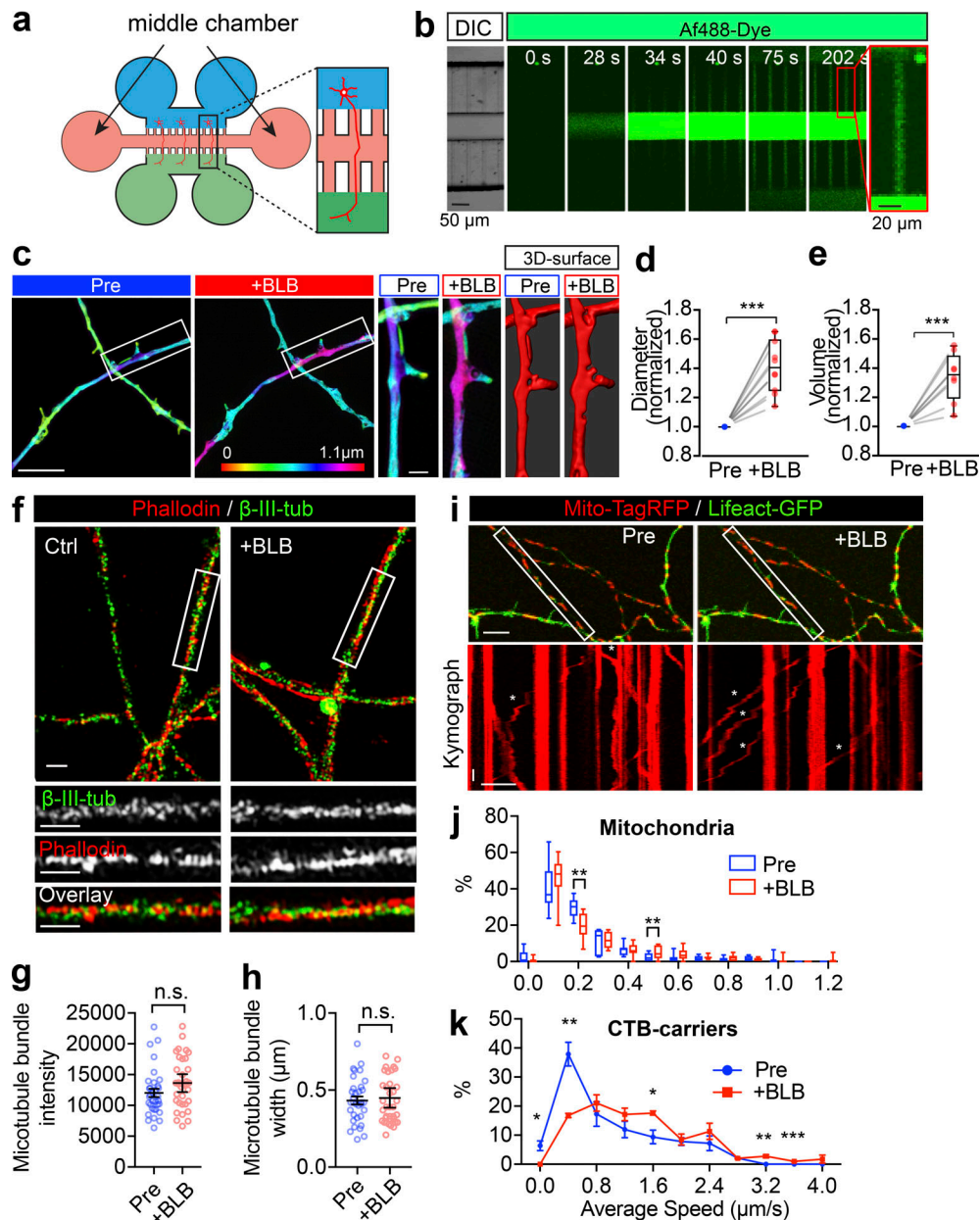


**Figure S6.   NM-II immunostaining closely correlates with the periodic actin rings along the axon. (a)** DIV14 rat hippocampal neurons were stained for endogenous F-actin (Phalloidin) and NM-IIB and imaged with dual-color 3D SIM. Boxed regions are shown with individual z-stack planes; periodic structure of NM-II and actin are indicated with arrows (green) and spots (red), respectively. **(b)** The NM-II and actin structures resolved with 3D SIM (right) were rendered into surface (right) using Imaris; boxed regions are magnified to show the accuracy of the rendering. The colocalization of the bracketed region is shown in the bottom panels. **(c)** Two-color SIM images of endogenous F-actin (phalloidin) and NM-II along the axons of control and Triton X-100–extracted axons. Scale bars = 1 µm. **(d–f)** Quantification of the percentage of axons bearing periodic actin rings (d), NM-II puncta number (e), and the percentage change in these two parameters (f) in control and Triton X-100–extracted axons (+Triton). Data represent mean ± SEM; *n* = 10 cells (control) and 9 cells (Triton X-100) from three independent cultures (**, P < 0.01; ***, P < 0.001, two-tailed unpaired *t* test).

Wang et al.
NM-II facilitates axonal trafficking and stability

**Journal of Cell Biology**   S5
https://doi.org/10.1083/jcb.201902001

Figure S7. **Short-term inactivation of NM-II causes the axon diameter expansion without affecting the microtubule structure or docking mitochondria. (a)** Schematic cartoon showing the structure of a 6-well microfluidic device. **(b)** Time-lapse images showing the distribution of Af488 dye in the middle chamber of a 6-well microfluidic device, indicating its restriction capacity. Scale bar = 50 µm. DIC, differential interference contrast microscopy. **(c)** Axons of DIV14 hippocampal neurons were treated with blebbistatin (10 µM) in the middle chamber for 90 min. Representative images of the 3D SIM time-lapse images of axons before (Pre) and after blebbistatin treatment (+BLB). Value of z axis is color-coded. Scale bar = 5 µm. Magnified images from the boxed regions and the corresponding Imaris surface rendered images are shown in panels on the right. Scale bars = 1 µm. **(d and e)** Quantification of changes in the axon diameter (d) and volume (e) before and after blebbistatin treatment. Data represent mean ± SEM. For diameter quantification, $n = 10$ (Pre) and 10 (+BLB) axons were analyzed; and for volume quantification, $n = 8$ axons (Pre), $n = 8$ (+BLB) axons were analyzed from three independent cultures (***, $P < 0.001$, two-tailed paired $t$ test). **(f)** DIV14 hippocampal neurons were treated with blebbistatin (10 µM, 60 min) and then fixed and stained for endogenous F-actin (phalloidin) and β-III-tubulin. Two-color SIM was used to resolve the actomyosin and microtubule structures, respectively. Scale bars = 1 µm. Quantification of changes in the microtubule intensity (g) and bundle width (h) in control and blebbistatin-treated axons. Data represent mean ± SEM. For intensity quantification, $n = 33$ (Pre) and 34 (+BLB) axons; for bundle width quantification, $n = 33$ axons (Pre) and $n = 37$ axons (+BLB) from three independent cultures (two-tailed paired $t$ test). **(i)** Hippocampal neurons transfected with mito-TagRFP (red) and Lifeact-GFP (green) were imaged at the level of their axons before and after blebbistatin treatment. Kymographs of mitochondria movements from boxed regions are shown in the lower panels. Asterisks indicate moving mitochondria. x bar = 10 µm; y bar = 10 s. **(j)** Quantification of average speed of mitochondria transport in i. The frequency distributions of the trajectories with different speeds are shown to note the effect on docking (0 and 0.1 µm/s) and moving mitochondria. Data represent mean ± SEM; $n = 7$ (Pre) and 8 (+BLB) axons from three independent cultures (**, $P < 0.01$, Student's $t$ test). **(k)** Quantification of average speed of CTB-positive carriers with and without blebbistatin treatment, as shown in transport in Fig. 7 a. The frequency distribution of the trajectories with different speed are shown to note the effect on slow and fast CTB carriers, respectively. Data represent mean ± SEM; $n = 3$ (Pre) and 3 (+BLB) experiments from three independent preparations (*, $P < 0.05$; **, $P < 0.01$; ***, $P < 0.001$, two-tailed Student's $t$ test). n.s., not significant.

Wang et al.
NM-II facilitates axonal trafficking and stability

Journal of Cell Biology S6
https://doi.org/10.1083/jcb.201902001

Video 1.   **Retrograde trafficking of Lysotracker-labeled cargoes in the axon terminals.** The retrograde trafficking of axonal cargoes labeled with Ly-sotracker deep red in the terminal chamber of the microfluidic device. From top to bottom: The Lysotracker carriers overlapping with bright-field signals and the masked carriers and trajectories are shown in the top panels, with the boxed ROIs being magnified in the bottom panels. Scale bar = 5 µm. Video is 100 frames/s.

Video 2.   **Retrograde trafficking of CTB-labeled endosomes.** The retrograde trafficking flux of axonal cargoes labeled with CTB in an axon channel of a microfluidic device. From top to bottom: The CTB-labeled cargoes, their trajectories, and the trajectories that overlapped with the bright-field signals are shown, respectively. Scale bar = 5 µm. Video is 100 frames/s.

Video 3.   **The transit of cargo causes a transient radial expansion of the axon.** The passage of cargo-associated black holes through the axon shafts caused an obvious mechanical stretching of the shafts, which are visualized in the Lifeact-GFP–expressing neuron (green) by time-lapse SIM. Black holes that are associated with moving cargoes are indicated with arrows. Scale bar = 2 µm. Video is 6 frames/s.

Video 4.   **Radial expansion of axonal actin rings caused by passages of lysosomal cargoes.** Time-lapse dual-color SIM images at 20-s intervals showing that diameter changes of periodic actin rings (SiR-actin) correlate with the passage of large lysosomal cargoes (Lysotracker red). The bracket segment is amplified in the bottom panels. Diameter changes are indicated with arrows. Scale bars = 1 µm (top); 5 µm (bottom). Video is 1 frame/s.

Video 5.   **Radial expansion of axonal actin rings caused by passages of lysosomal cargoes.** Time-lapse dual-color SIM images at 20-s intervals showing that diameter changes of periodic actin rings (SiR-actin) correlate with the passage of large lysosomal cargoes (Lysotracker red). The bracket segment is amplified in the bottom panels. Diameter changes are indicated with arrows. Scale bars = 1 µm (top); 5 µm (bottom). Video is 1 frame/s.

Video 6.   **Radial expansion of axonal plasma membrane caused by passages of axonal cargoes.** Time-lapse dual-color SIM images at 20-s intervals showing that diameter changes of axonal plasma membrane (CellMask Deep Red) correlate with the passage of large lysosomal cargoes (Lysotracker red). Diameter changes of axonal plasma membrane are indicated with arrows. Scale bar = 1 µm. Video is 1 frame/s.

Video 7.   **Radial expansion of axonal plasma membrane caused by passages of axonal cargoes.** Time-lapse dual-color SIM images at 20-s intervals showing that diameter changes of axonal plasma membrane (CellMask Deep Red) correlate with the passage of large lysosomal cargoes (Lysotracker red). Diameter changes of axonal plasma membrane are indicated with arrows. Scale bar = 1 µm. Video is 1 frame/s.

Video 8.   **Dynamic radial contractility of periodic actin rings along axons.** Time-lapse 2D SIM images at 20-s intervals showing the diameter changes of periodic axonal actin rings periodic actin rings labeled with SiR-actin. Four bracket segments were amplified in the right panels. Diameter changes are indicated with arrows. Scale bars = 1 µm (left); 5 µm (right). Video is 1 frame/s.

Video 9.   **Retrograde trafficking of CTB-labeled endosomes with short-term blebbistatin treatment.** The retrograde trafficking flux of axonal cargoes labeled with CTB in an axon channel of a microfluidic device after treatment with 10 µM blebbistatin for 60 min. From top to bottom: The CTB-labeled cargoes, their trajectories, and the trajectories that overlapped with the bright-field signals were shown, respectively. Scale bar = 5 µm. Video is 100 frames/s.

Video 10.   **Retrograde trafficking of Lysotracker-labeled endosomes after blebbistatin treatment.** The retrograde trafficking of axonal cargoes labeled with Lysotracker in the terminal chamber of a microfluidic device after treatment with 10 µM blebbistatin for 60 min. From top to bottom: The Lysotracker carriers overlapping with bright-field signals and the masked carriers and trajectories are shown in the top panels, with the boxed ROIs being magnified in the bottom panels. Scale bar = 5 µm. Video is 100 frames/s.